

Drought-induced vertical displacements and water loss in the Po river basin (Northern Italy) from GNSS measurements

Francesco Pintori¹ and Enrico Serpelloni²

¹Dipartimento di Fisica e Astronomia, Settore di Geofisica, Università di Bologna

²Istituto Nazionale di Geofisica e Vulcanologia

June 6, 2023

Abstract

We study vertical ground displacement time-series from GNSS stations in the Po river basin to measure deformation signals associated with the severe drought occurring since 2021 and estimate the spatial distribution of water loss. The detection of vertical ground displacement trend changes allows us to extract a spatially correlated signal that follows the Po level trend changes and SPEI-12 drought index. GNSS stations in the basin mostly underwent uplift, up to 7 mm, since 2021, which corresponds to ~80 Gtons of water loss. Compared to GLDAS and GRACE, the GNSS results show a similar temporal evolution of water content, but a different spatial distribution. Our study indicates that using dense GNSS networks is an effective way to monitor long-term changes in water storage even in small water basins and serve as a reliable indicator of drought severity.

15 **Abstract**

16 We study vertical ground displacement time-series from GNSS stations in the Po river basin to
17 measure deformation signals associated with the severe drought occurring since 2021 and
18 estimate the spatial distribution of water loss. The detection of vertical ground displacement
19 trend changes allows us to extract a spatially correlated signal that follows the Po level trend
20 changes and SPEI-12 drought index. GNSS stations in the basin mostly underwent uplift, up to
21 7 mm, since 2021, which corresponds to ~80 Gtons of water loss. Compared to GLDAS and
22 GRACE, the GNSS results show a similar temporal evolution of water content, but a different
23 spatial distribution. Our study indicates that using dense GNSS networks is an effective way to
24 monitor long-term changes in water storage even in small water basins and serve as a reliable
25 indicator of drought severity.

26 **Plain Language Summary**

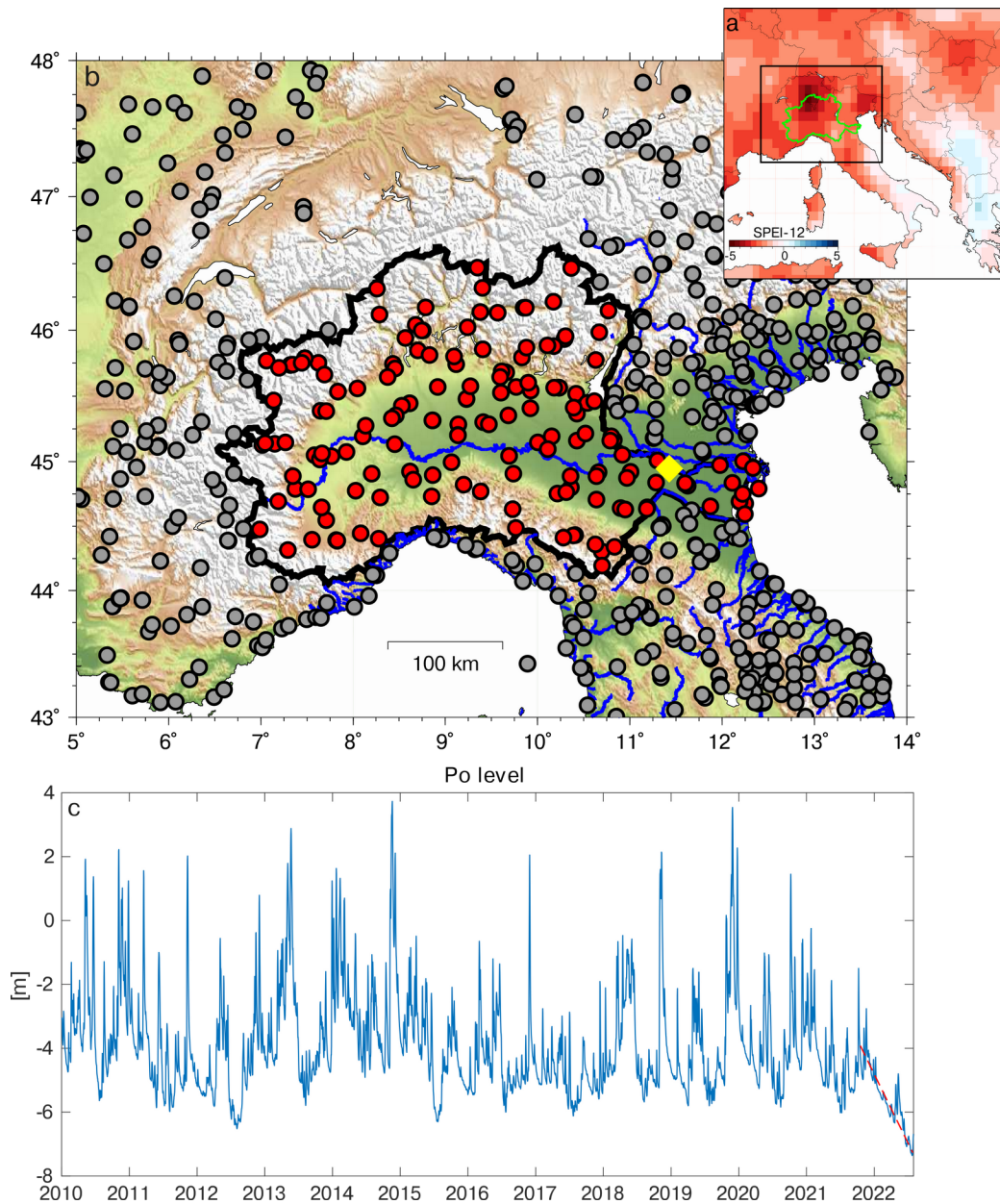
27 This study looks at the way the ground moves up and down in the Po river basin, in northern
28 Italy, using Global Navigation Satellite System (GNSS) stations. We measure how much
29 water was lost during a big drought in the area since 2021. We find that the GNSS stations
30 show that the ground mostly moved upwards since 2021, which means that water was being
31 lost. We estimate that about 80 billion tons was lost during that time, in agreement with other
32 ways of measuring terrestrial water variations. This study shows that GNSS stations can be an
33 alternative way to measure how much water is being lost during drought in small areas and
34 common vertical displacement signals are a good approximation of drought indexes.

35 **1 Introduction**

36 Drought is one of the most complex recurring natural disasters, defined by a deficiency
37 of precipitations that causes prolonged water scarcity. Failure to manage drought risk has the
38 potential to have dire consequences for people, livelihoods, economy and ecosystems. During
39 the summer of 2022 Italy faced a severe drought, where the dry conditions were related to a
40 persistent lack of precipitation since December 2021. The level of the largest Italian river, the
41 Po, has been significantly decreasing since the summer of 2021 (Fig. 1). Several regions
42 declared a state of emergency, and drinking water has been rationed in hundreds of
43 municipalities in northern Italy. Figure 1 shows a map of the Standardised Precipitation-

44 Evapotranspiration Index (SPEI-12, Vicente-Serrano et al. 2010), which quantifies the drought
 45 level of the last 12 months taking into account both precipitation and potential
 46 evapotranspiration.

47



48 **Figure 1. a) SPEI-12 computed on August 2022. b) The study area: the black line**
 49 **represents the Po river (thick blue line) basin; the dots show the positions of the GNSS**
 50 **stations used in the analysis, the reds are the ones inside the basin, the gray the ones**
 51 **outside; the yellow diamond shows the location of the Po level measurement point. c) Po**
 52 **river level changes. The rapid level drop between 2021 and 2022 is shown by the red**
 53 **dashed line.**

54 The effects of droughts are particularly dangerous in the Po river basin for various
55 reasons: drought threatens the crops in the Po Valley, which are around 40% of the total food
56 produced in Italy, and impacts energy production, since a reduced river flow causes
57 deficiencies in hydropower generation and cooling of thermal plants (Boyko et al., 2022).

58 Due to global warming, more frequent and severe droughts are likely to occur in the
59 next future (Boyko et al., 2022). For this reason, while it is necessary to measure and monitor
60 variations in terrestrial water storage (TWS) in order to evaluate the best policies to address
61 the problems caused by water scarcity, it is difficult to get measurements of all the TWS
62 components, which include groundwater, surface water, vegetation and soil moisture, ice and
63 snow. Piezometers, for example, effectively monitor groundwater level variations but not the
64 other water storage components, and evaluating the water volume changes from them is not
65 straightforward. On the other hand, the Global Land Data Assimilation System (GLDAS)
66 model provides daily variations of the soil moisture and snow water equivalent, but it can not
67 take into account the groundwater stored more than 2 m below the surface (Argus et al., 2014;
68 Jiang et al., 2021). TWS can also be estimated using Gravity Recovery and Climate
69 Experiment (GRACE) measurements, which allow modeling water storage changes by
70 inverting the spatiotemporal variations of the Earth's gravity field. Unlike GLDAS, all the
71 components of TWS are taken into account by GRACE, nonetheless its spatial resolution
72 (300-400 km) and its temporal resolution (monthly) are too coarse for many regional or local
73 studies (Fu et al., 2015; Knappe et al., 2019).

74 TWS variations are indirectly detectable not only through gravity data but also by
75 measuring ground displacements through geodetic observations: a water content increase
76 causes an increasing load on the Earth surface, which subsides elastically; while when the
77 water content decreases the crust moves upward because of the water content decrease. Global
78 Navigation Satellite System (GNSS) measurements, for example, provide daily measurements
79 of ground displacements, at mm precisions, that can be used to measure ground deformation
80 associated with TWS variations. Argus et al. (2014) inferred the spatial distribution of the
81 TWS seasonal amplitude, expressed in terms of equivalent water height (EWH), by inverting
82 the seasonal vertical displacements of the ground in California. Fu et al. (2015) estimated
83 TWS variations from GNSS measurements of vertical displacement in Washington and
84 Oregon, finding that the largest seasonal variations of water content were localized in the

85 mountain areas. GNSS displacements have been inverted to estimate the TWS also by Jin and
86 Zhang (2016) in the southwestern United States, by Zhang et al. (2016) over the Yunnan
87 Province in China and by Ferreira et al. (2019) in the entire South America.

88 Carlson et al. (2022) computed TWS in California using a joint inversion method
89 combining the GRACE products with the results of the inversion of GNSS data, taking
90 advantage of the dense spatial distribution of GNSS data together with GRACE's ability to
91 provide regional closure of the water budget.

92 In this work we estimate the amount of water loss in the Po river basin, extending
93 $\sim 7.4 \cdot 10^5$ km², by inverting vertical ground displacements measured by continuous GNSS
94 stations. We consider stations inside the basin, but also stations located within 1° from the
95 basin boundaries, in order to reduce inversion artifacts near the boundaries of the study region
96 (Fu et al. 2015). We focus on long-term, inter-annual, changes, rather than seasonal (i.e.,
97 annual) variations, by modeling displacement time-series looking for trend changes in the
98 vertical component, with particular focus on the most recent and severe 2021-2022 drought.

99 In Section 2 we describe the GNSS data used and the methods applied to analyze the
100 vertical displacement time series; in Section 3 we show the relationship between geodetic and
101 hydrological observations and provide a quantitative estimation of the evolution of the TWS.
102 In Section 4 we discuss the results, in light of alternative estimates of water storage variations.

103 2 Data and Methods

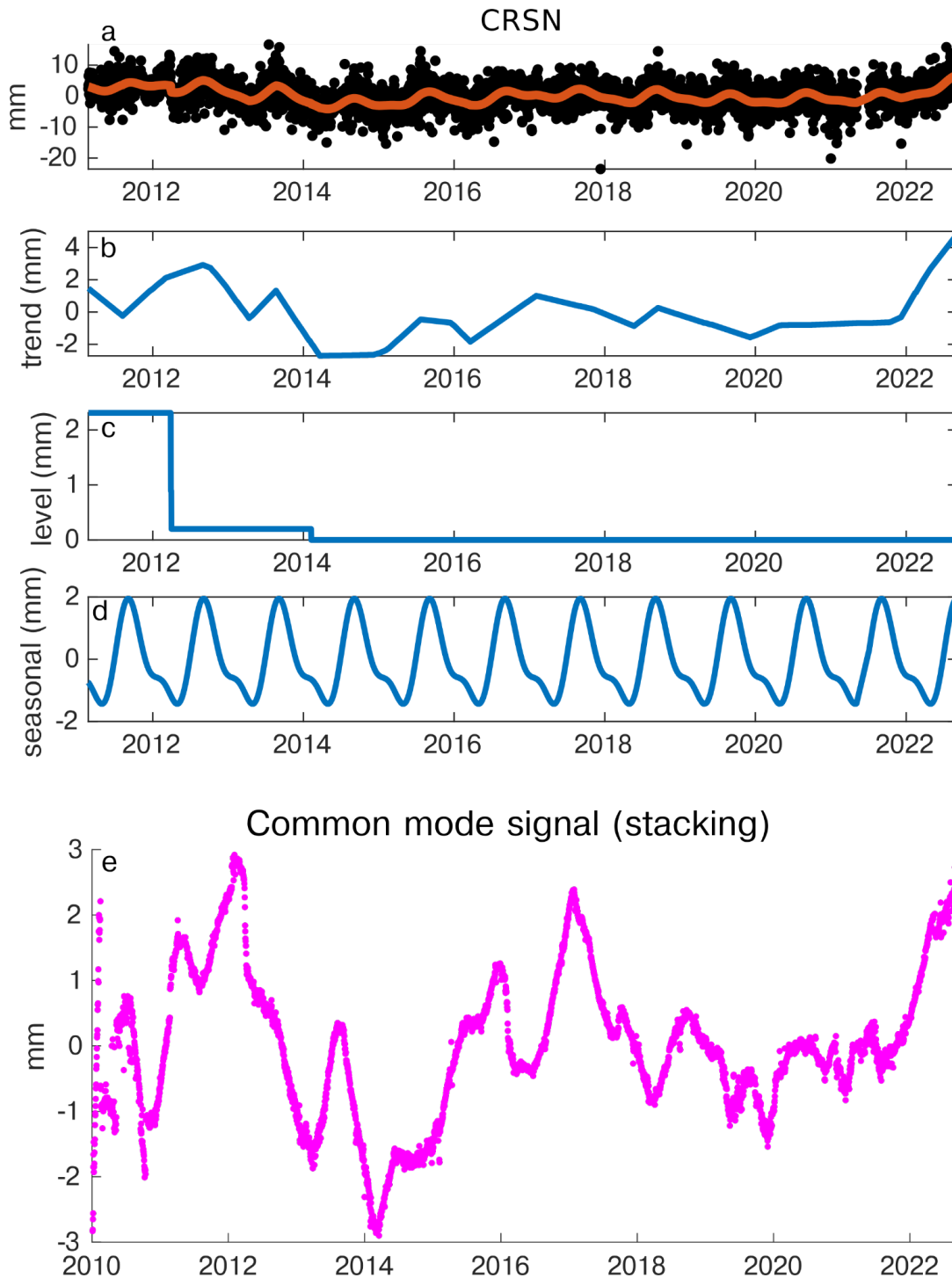
104 We consider ~180 daily GNSS vertical ground displacement time series from January,
 105 2010 to September, 2022 of continuous stations located in the Po river basin (see Fig. 1). We
 106 also include in the analysis ~280 stations located within 1° of the catchment limits. This is part
 107 of a larger geodetic solution encompassing the whole Euro-Mediterranean region, obtained
 108 following the approach detailed in Serpelloni et al. (2022). We remove the long-term linear
 109 trend from the time series using the Median Interannual Difference Adjusted for Skewness
 110 (MIDAS) estimator (Blewitt et al. 2016) and filter the contribution of the non-tidal
 111 atmospheric loading (NTAL), as suggested by White et al. (2022), since they can produce
 112 displacements of several millimeters at daily-weekly timescales that can interfere with the
 113 hydrological signal. The NTAL-induced vertical displacements are evaluated from the daily
 114 0.5° x 0.5° gridded solution of the Earth-System-Modeling Group at the German Research
 115 Center for Geosciences (Dill and Dobsław, 2013) and its contribution in each site is calculated
 116 considering the nearest grid point where the displacements associated with NTAL are
 117 computed.

118 The resulting GNSS vertical displacements time series are then analyzed using a trend
 119 filtering approach, which performs an extensive analysis using a L1 norm regularization
 120 model to identify the seasonal components, offsets and linear trend changepoints in the GNSS
 121 time series (Wu et al. 2018). The piecewise trend x is estimated by minimizing the weighted
 122 sum objective function:

$$123 \quad (1/2)\|y - x - s - w\|_2^2 + \lambda \|D^{(2)}x\|_1 + \rho \|1 + D^{(1)}w\|_1$$

124 where y is the original time series, w indicates the level component associated with the
125 offsets, s is the seasonal term, $\|\cdot\|_1$ represents the L1 norm and $D^{(n)}$ are the n -th difference
126 matrix defined as in Wu et al. (2018). λ and ρ are positive parameters controlling the knots of
127 the estimation trend and the frequency of level shifts, respectively (we choose $\lambda=2000$ and $\rho=$
128 80). Figure 2 shows an example of output of this analysis. Focusing on transients and
129 interannual variations, we only consider the extracted piecewise trends, not the seasonal terms
130 having annual and semi-annual frequencies. For some stations level changes (i.e., offsets) not
131 associated with tectonic events or equipment changes are highlighted, which mostly represent
132 fast variations in ground displacements (see Fig. 2 in 2012). For this reason, in the further
133 steps we consider the piecewise trend as the sum of the trend and level components. As it can
134 be seen in Fig. 2, there is an increase in uplift starting from 2021, which is a common feature
135 in GNSS stations within the Po river basin. Fig. 2e shows the stacking of the vertical
136 piecewise trend time-series for all stations analyzed, which is performed by averaging, for
137 each epoch, the residuals of all the time series resulting by removing the mean and linear trend
138 terms. In order to better characterize the spatial distribution of this deformation signal, we use
139 a multivariate statistical approach, similarly to what is used for tectonic deformation studies
140 (Kositsky and Avouac, 2010; Gualandi et al. 2014).

141



142
 143 **Figure 2. Example of GNSS time series decomposition performed using the L1-norm**
 144 **trend filtering approach. In a) the black dots represent the original time series, the red**
 145 **line the model obtained as the sum of the trend (b), level (c) and seasonal component (d).**
 146 **Panel (e) shows the result of the stacking on the piecewise vertical trends of all the**
 147 **stations inside the Po river basin.**

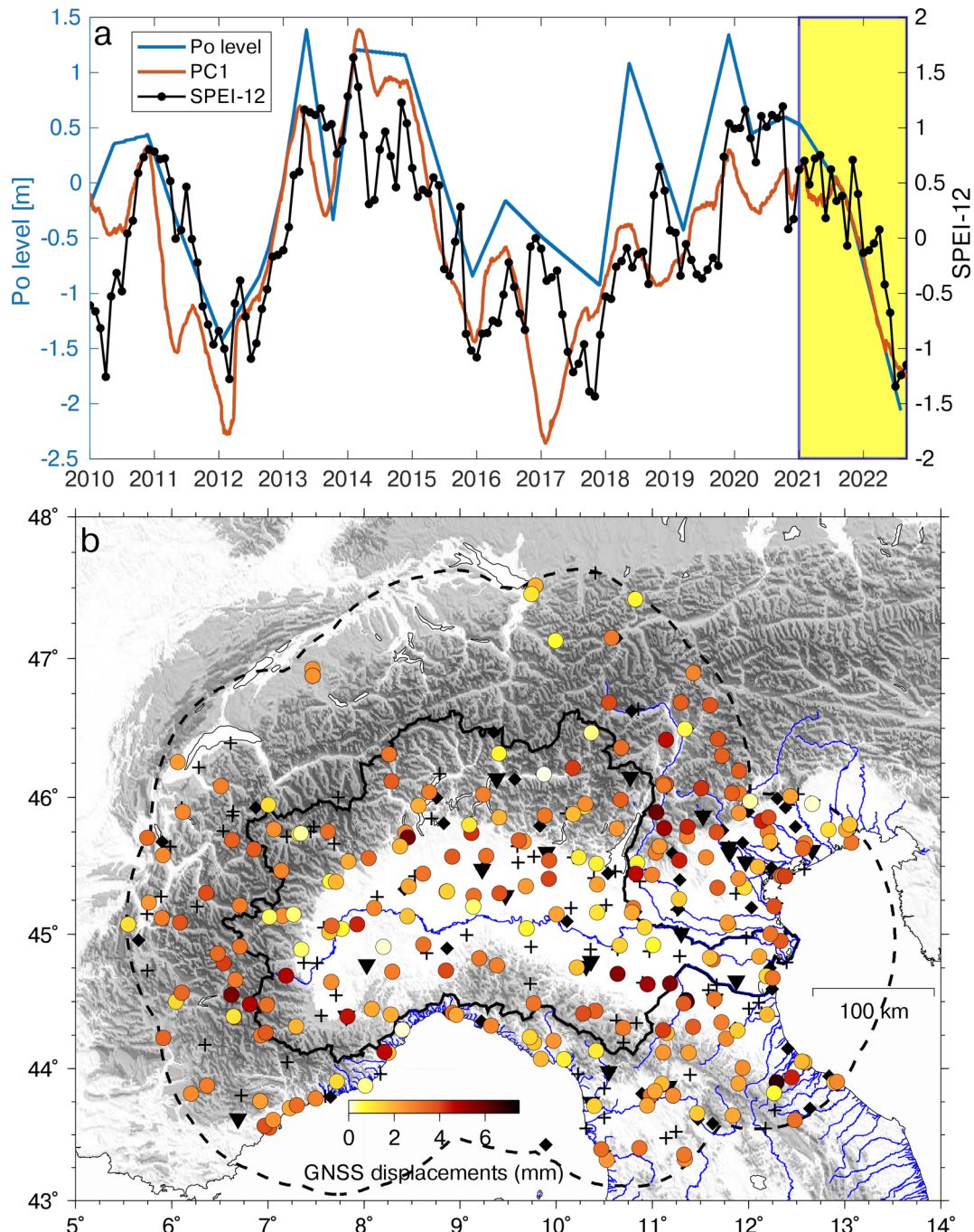
148 **3 Results**

149 3.1 Comparison between geodetic and hydrological measurements

150 We adopt an approach similar to the one described in Jiang et al. (2022), but we use as
151 input of a principal component analysis (PCA) the piecewise vertical trends described in the
152 previous section, rather than the raw time-series. We decompose the dataset using one PC in
153 order to identify the most important common signal of the GNSS stations in the Po basin and
154 retrieve its spatial pattern (i.e., amplitude and sign). However, the first principal component
155 (PC1) obtained performing a PCA using 2 or 3 components is almost identical to the PC1
156 obtained performing a one-component decomposition, both in terms of temporal evolution
157 (Fig. S1) and spatial distributions (Fig. S2).

158 The temporal evolution of PC1 (Fig. 3A) well resembles the common mode signal
159 resulting from a stacking of the vertical trend time-series for all stations (Fig. 2e and Fig. S3).
160 However, the advantage of the PCA is to provide the spatial information on the displacement
161 amplitudes (Fig. S2A).

162 We compare the temporal evolution of PC1 with the SPEI-12 index value, averaged
163 over the Po river basin, and with the Po river level measurements provided by the Regional
164 Agency for Environmental Protection of Veneto region (ARPAV;
165 <https://wwwold.arpa.veneto.it/arpavinforma/bollettini/dati-storici>, Last Access: 20-12-2022).
166 The Po river level time series is filtered adopting the same approach used for the GNSS time-
167 series, and retaining only the piecewise trend component (Fig. S4). On the other hand, SPEI-
168 12 time series does not contain annual variations, since the index is computed as an anomaly
169 over 12 months, then the time series has not been filtered. Figure 3A shows that the geodetic,
170 climatic and hydrological time series are highly temporally correlated.



171 **Figure 3. a) Comparison between the PC1 temporal evolution, the SPEI-12 index and the**
 172 **Po river level. Since PC1 is obtained from detrended GNSS time series, Po river level and**
 173 **SPEI-12 have also been detrended for consistency. b) Vertical displacements associated**
 174 **with PC1 during the 2021.00 (January, 2021) - 2022.67 (September, 2022) time interval**
 175 **(yellow panel). The dashed line represents the boundary of the Po river basin, extended**
 176 **by 1°. Black triangles indicate the 21 stations excluded because they show negative**

177 **displacements; black crosses represent sites with more than 75% of missing data and**
178 **black diamonds the stations with no records after 2021.0.**

179 The vertical displacements associated with PC1 from 2021.00 to 2022.67 are shown in
180 Fig. 3B. Most of the stations show positive values (uplift), in accordance with the hypothesis
181 that in dry periods, when the water load is reduced, the GNSS stations record uplift, while in
182 wet periods the water load increases causing a downward motion of the Earth's surface. We
183 find that this is not true for 21 sites, which show an opposite behavior (black triangles in Fig.
184 3B). Maximum uplift, of the order of 7 mm, is observed in the south-eastern portion of the
185 basin and in the northern portion of the Po basin, which correspond to uplift rates, in the
186 considered two years, that are much faster than the long-term ones (e.g., Pintori et al., 2022).

187 3.2 Inversion of vertical ground displacements

188 The displacements associated with PC1 are inverted using the approach described in
189 Jiang et al. (2022), which estimates water storage variations assuming an elastic response of
190 the Earth to the hydrological load. In order to avoid misinterpretation of the spatial variations
191 of the water storage changes, we exclude from the inversion the 21 stations showing negative
192 vertical displacements (i.e., subsidence, Fig. S5) in the investigated time interval that,
193 following Carlson et al. (2022), are possibly affected by poroelastic processes, causing vertical
194 displacements in the opposite direction compared to the elastic ones. We also exclude from the
195 inversion the GNSS stations that have no observations recorded in the 2021.00-2022.67 time-
196 span (i.e., do not register displacements potentially associated with the last drought episode
197 investigated in this work). The total number of stations used for the inversion is then 250.

198 The relationship between the vertical displacements measured by GNSS x and the
199 water mass load u , expressed as EWH, is

$$200 \quad x = Gu$$

201 where G is the Green's function matrix using load Love numbers of the preliminary reference
 202 earth model (PREM) (Dziewonski and Anderson, 1981) as commonly used in many recent
 203 works (e.g. Carlson et al. 2022, Jiang et al. 2021). The final solution for the daily estimates of
 204 EWH changes u is

$$205 \quad u = (G^T G + \alpha^2 L^T L)^{-1} G^T x$$

206 where L is the Laplacian smoothing matrix and α is the smoothing factor controlling the
 207 relative weight between model roughness and data misfit.

208 We invert the displacements associated with PC1 to estimate EWH on a $0.25^\circ \times 0.25^\circ$
 209 grid. We choose $\alpha = 0.0034$, which is the minimum in the line showing the relation between the
 210 sum of squared residuals from cross-validation (CVSS) and the smoothing factor (Fig. S6),
 211 and use 4 neighbor points for calculating the Laplacian matrix during the least-squares
 212 inversion. Fig. 3A shows the temporal evolution of the EWH averaged over the study area,
 213 while Fig. 3B is a map of the EWH variations that occurred in the 2021.00 - 2022.67 time
 214 interval (yellow box in Fig.3A).

215 Text S1 presents the results of checkerboard tests, showing that our inversion is well
 216 resolved at the spatial resolution of $1^\circ \times 1^\circ$.

217 **4 Discussion**

218 We compare the EWH obtained by inverting the GNSS displacements (EWH_{gnss}) with
 219 surface water content from GLDAS (SWC) and with Liquid Water Equivalent Thickness
 220 (LWE) from GRACE.

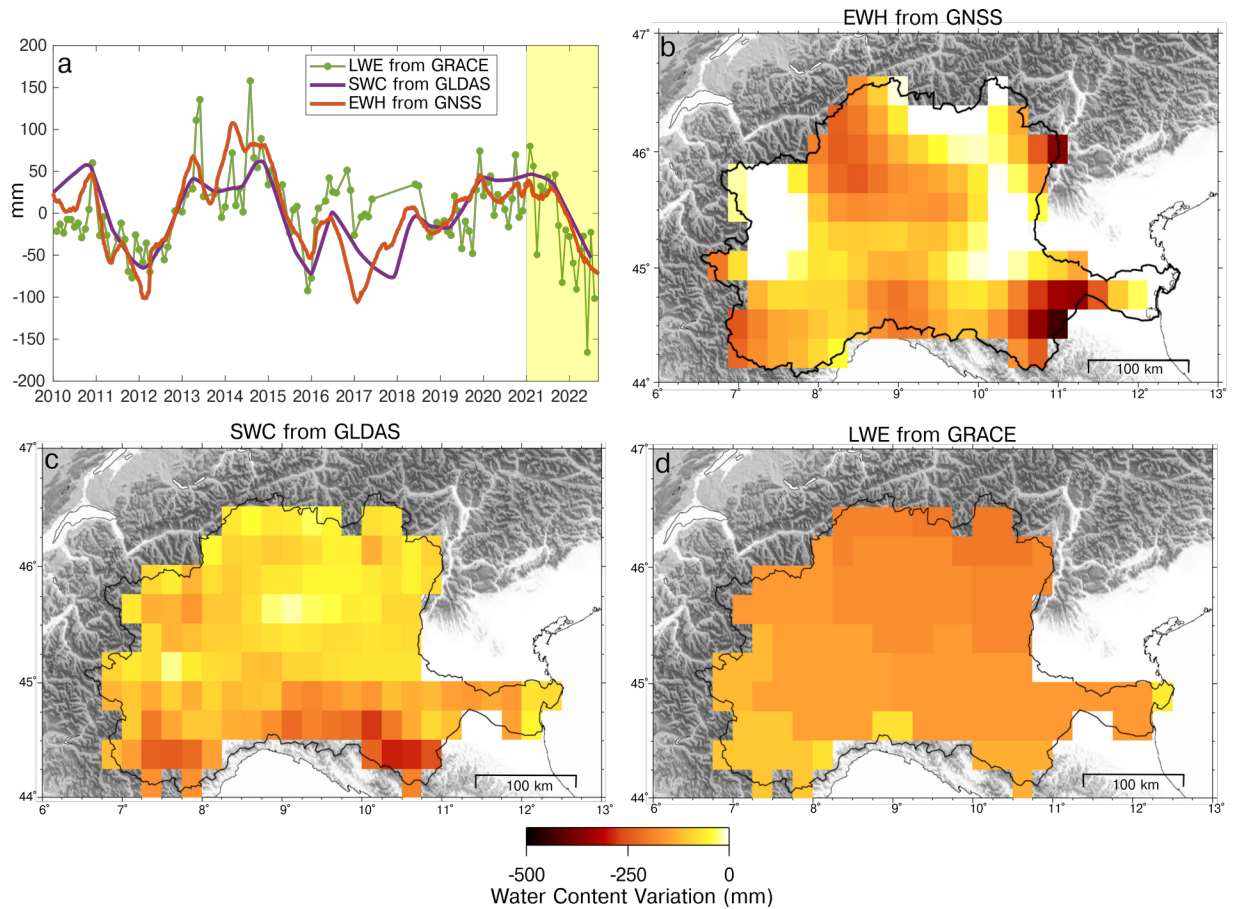
221 The GLDAS products provide the soil moisture content in the first 2 m of the
 222 subsurface, the snow depth water equivalent, the plant canopy surface water and the root zone
 223 soil moisture (Rodell et al., 2004). We consider as SWC the sum of these four components,
 224 which are provided as $0.25^\circ \times 0.25^\circ$ gridded dataset and 3-hours temporal resolution, which are
 225 transformed into daily time series by averaging the 3-hourly time series to make them
 226 consistent with the daily resolution of EWH_{gnss} .

227 LWE is computed using the GRACE and GRACE-FO RL06 Mascon solutions from
228 the Center for Space Research (Save et al., 2016; Save, 2020). While the data are provided in a
229 grid with the same size as the GLDAS one, which corresponds to a resolution of about 25 km,
230 the current resolution is 300-400 km. The temporal resolution of LWE data is monthly and
231 data are missing in correspondence with the gap between the GRACE and GRACE-FO
232 missions, which results in a 11 months gap, from July 2017 to May 2018.

233 The GLDAS products allow an estimate of the water content with a better nominal
234 spatial resolution of $EW_{g_{nss}}$, even though the disadvantage is that GLDAS does not take into
235 account groundwater. Importantly, while the GLDAS nominal spatial resolution is 0.25° , its
236 effective resolution may be different due to the assimilation process and the interpolation
237 techniques used to generate gridded datasets. Furthermore, the nominal spatial resolution of
238 GLDAS may not represent the true spatial variability of soil moisture in a context such as the
239 Po river basin, characterized by high topographic gradients. The correct determination of the
240 soil types in regions characterized by heterogeneous landscapes, elevation and land cover, in
241 fact, is complex and this can lead to errors in soil moisture modeling (Bi et al., 2016).

242 LWE takes into account all TWS components, but with a spatial and temporal
243 resolution much poorer than $EW_{g_{nss}}$. We point out that while $EW_{g_{nss}}$ is inverted on a
244 $0.25^\circ \times 0.25^\circ$ grid, the results of the checkerboard test show that the actual spatial resolution is
245 $\sim 1^\circ$, corresponding to about 100 km (Section S1 of the Supporting Information). This is
246 consistent with the resolution achieved by Zhang et al. (2016) in the Yunnan region of China
247 and by Fu et al. (2015) in Washington and Oregon. The high spatial density of the southern
248 California GNSS network allowed Carlson et al. (2022) to reach a spatial resolution of 80 km,
249 while when considering larger study areas as in Borsa et al. (2014) and in Ferreira et al. (2019)
250 the spatial resolution decreases to 200-300 km.

251 We filter the annual and semiannual signals in SWC time series using the same
252 approach used for GNSS displacement and Po river level measurements (see Fig. S8), and
253 apply a PCA using one PC on the trend components. Because of the monthly temporal
254 resolution of the GRACE products, LWE data are analyzed using a slightly different strategy,
255 removing the annual and semiannual components from the original time series instead of
256 estimating the trend components, as done for GNSS and GLDAS time-series. In fact, the trend
257 variations observed in $EW_{g_{nss}}$ occur also at a monthly timescale, but the temporal resolution
258 of LWE is also monthly, so it is unnecessary to estimate the LWE trend variations. As for the
259 GLDAS and GNSS datasets, the filtered time series are analyzed with a PCA with one PC.
260 Fig. 4a shows the temporal evolutions of the basin-averaged water content expressed as
261 $EW_{g_{nss}}$, SWC from GLDAS and LWE from GRACE, while Fig. 4b-d shows the spatial
262 distributions of water loss from January, 2010 to September, 2022 (yellow box in Fig. 4a),
263 estimated from GNSS, GLDAS and GRACE, respectively.



264 **Figure 4. a) Comparison among the temporal evolutions of the regional-averaged water**
 265 **content expressed as EWH_{gnss} (red), SWC (purple) and LWE (green). Since EWH is**
 266 **obtained from GNSS detrended data; both GLDAS and GRACE data have also been**
 267 **detrended for consistency. b) Water loss occurred in the 2021.00 - 2022.67 time interval**
 268 **in terms of EWH from GNSS, c) SWC from GLDAS and d) LWE from GRACE.**

269 The temporal evolution of the basin-averaged water content estimated by the three
 270 models is very similar, especially between EWH_{gnss} and SWC (Fig. 4a), suggesting that the
 271 water storage variations may be dominated by its superficial content, captured by GLDAS.
 272 The spatial distribution of the water loss occurring in the 2021.00 - 2022.67 time interval (Fig.
 273 4b-d) is different depending on the considered dataset; nonetheless, averaging on the Po basin
 274 surface, we obtain water loss values of the order of about 80, 82 and 115 Gtons from GNSS,
 275 GLDAS and GRACE, respectively in this period.

276 The poor spatial resolution of GRACE measurements makes LWE spatial distribution
277 “smoother” than the other two datasets and not able to detect concentrations of water loss at
278 the scale of the Po river basin. Both SWC and EWH_{gnss} show the largest values in the southern
279 portion of the basin, but EWH_{gnss} is large also in the north-central portion of the basin, in
280 agreement with the SPEI-12 map (Fig. 1), and very small in the eastern and western portions.
281 The reason for the observed spatial discrepancy can be a consequence of the GLDAS
282 limitations in resolving the spatial distribution of the water loss in the mountain sectors. It is
283 also worth considering that GNSS vertical displacements can contain signals that might cause
284 an incorrect estimation of the water content. In fact, the inversion is made on the
285 displacements reconstructed by the PC1. This statistical approach allows us to identify a
286 common displacement signal that has the same temporal evolution in all the GNSS stations,
287 but different amplitudes. The amplitude associated with this signal might be imprecise,
288 especially in GNSS sites characterized by noisy time-series or for stations affected by local
289 processes.

290 Importantly, estimates of water loss values depend on the Green’s function used to
291 invert the displacements data. Several authors (e.g., Argus et al., 2017; Chanard et al., 2014),
292 point out that a gravitating, spherical Earth model is preferred in this context, since non
293 gravitating, half-space models, can understate elastic vertical displacements up to a factor of
294 2.5. Moreover, the results are not very sensitive to the Earth's structure: assuming two
295 different models for the Earth, PREM and the Gutenberg Bullen A Earth structure (Farrell,
296 1972), Argus et al. (2017) find that the difference between the displacements caused by a 450
297 $\text{km} \times 60 \text{ km}$ load is only 4%.

298 **5 Conclusions**

299 We analyze vertical ground displacements from GNSS stations located in the Po river
300 basin, a significant European district with industrial and agricultural settlements. Our study
301 demonstrates that changes in vertical trends respond to meteo-climatic forcing and serve as a
302 reliable, near real-time, independent approximation of drought indexes. During the drought
303 that has affected the region since 2021, we observe a regional uplift signal. This uplift reaches
304 values of up to 7 mm and exhibits spatial variations across the area. We interpret this
305 phenomenon as a result of variable water loss and subsequent reduced load, enabling us to
306 estimate the spatial distribution of EWH. GNSS observations indicate that an estimated
307 average of approximately 80 Gtons of water was lost in the Po river basin from 2021 to the
308 end of summer 2022. This estimate aligns with values obtained from GLDAS but is lower than
309 the estimate derived from GRACE. Additionally, while the temporal evolution of EWH
310 estimated by GNSS, GLDAS, and GRACE shows similarities, the spatial patterns differ
311 significantly.

312 Our findings are also relevant for studying active tectonics and geodynamics. The
313 Apennines and Alps, in fact, exhibit long-term uplift signals resulting from various multiscale
314 processes (Sternai et al., 2019). Accounting for the hydrological origins of trend variations is
315 crucial to improve accuracy and prevent misinterpretation of transient signals or biases in
316 velocity estimates, especially in case of short time-series.

317 Future research will integrate GNSS with InSAR data to improve the spatial resolution
318 of EWH to a few tens of meters, as demonstrated by Ghorbani et al. (2022). This integration
319 would enhance our understanding of the phenomenon and provide more detailed information
320 on water loss and recharge dynamics.

321 **Acknowledgments**

322 We thank GNSS data providers (see Serpelloni et al. 2022 for references), and in
323 particular private networks providers. This study has been partially developed in the
324 framework of the “CLYPEA-Innovation Network for Future Energy” framework, “subsoil
325 deformations” project, funded by the Italian Ecologic Transition Ministry (MITE). Some of

326 the figures are created using the Generic Mapping Tools (GMT) software (Wessel et al.,
327 2013).

328 **Open Research**

329 The EWH is estimated by inverting the GNSS data using the GNSS2TWS software
330 (<https://github.com/jzshhh/gnss2tws>).

331 The trend filtering on the GNSS vertical displacements time series is performed using
332 the L1tool software (<https://github.com/wudingcheng/l1tool>).

333 The stacking of the GNSS time series is performed using the GNSS_TS_NRS code
334 (<https://github.com/CL-Xiong/GNSS-TS-NRS>, He et al., 2020).

335 GLDAS data was downloaded from
336 https://disc.gsfc.nasa.gov/datasets/GLDAS_NOAH025_3H_2.1/summary?keywords=GLDAS.

337 GRACE data was downloaded from <http://www2.csr.utexas.edu/grace>.

338 SPEI-12 data was downloaded from
339 <https://spei.csic.es/map/maps.html#months=1#month=0#year=2023GNSS>.

340 GNSS time series data are available from
341 <https://doi.pangaea.de/10.1594/PANGAEA.958598>.

342 The maps have been made using the GMT software (Wessel et al. 2019).

343 **References**

344 Argus, D. F., Fu, Y., & Landerer, F. W. (2014). Seasonal variation in total water storage in
345 California inferred from GPS observations of vertical land motion. *Geophysical Research*
346 *Letters*, 41(6), 1971–1980. <https://doi.org/10.1002/2014GL059570>

347 Argus, D. F., Landerer, F. W., Wiese, D. N., Martens, H. R., Fu, Y., Famiglietti, J. S., et al.
348 (2017). Sustained water loss in California's mountain ranges during severe drought from
349 2012 to 2015 inferred from GPS. *Journal of Geophysical Research: Solid Earth*, 122(12),
350 10,559-10,585. <https://doi.org/10.1002/2017JB014424>

351 Beaudoin, H. & Rodell, M. NASA/GSFC/HSL (2020), GLDAS Noah Land Surface Model
352 L4 3 hourly 0.25 x 0.25 degree V2.1, Greenbelt, Maryland, USA, Goddard Earth Sciences
353 Data and Information Services Center (GES DISC), Accessed: [10/10/2022],
354 <https://doi.org/10.5067/E7TYRXPJKWOQ>

- 355 Bi, H., Ma, J., Zheng, W., & Zeng, J. (2016). Comparison of soil moisture in GLDAS model
356 simulations and in situ observations over the Tibetan Plateau. *Journal of Geophysical*
357 *Research: Atmospheres*, 121(6), 2658–2678. <https://doi.org/10.1002/2015jd024131>
- 358 Blewitt, G., Kreemer, C., Hammond, W. C., & Gazeaux, J. (2016). MIDAS robust trend
359 estimator for accurate GPS station velocities without step detection. *Journal of*
360 *Geophysical Research. Solid Earth*, 121(3), 2054–2068.
361 <https://doi.org/10.1002/2015JB012552>
- 362 Boyko, O., Reggiani, P., & Todini, E. (2022). Post-processing climate projections of
363 precipitation for the Po river basin: will Italy's North become water-constrained?
364 *Hydrology Research*, 53(11), 1414–1427. <https://doi.org/10.2166/nh.2022.063>
- 365 Carlson, G., Werth, S., & Shirzaei, M. (2022). Joint inversion of GNSS and GRACE for
366 terrestrial water storage change in california. *Journal of Geophysical Research. Solid*
367 *Earth*, 127(3), e2021JB023135. <https://doi.org/10.1029/2021JB023135>
- 368 Chanard, K., Avouac, J. P., Ramillien, G., & Genrich, J. (2014). Modeling deformation
369 induced by seasonal variations of continental water in the Himalaya region: Sensitivity to
370 Earth elastic structure. *Journal of Geophysical Research: Solid Earth*, 119(6), 5097–
371 5113. <https://doi.org/10.1002/2013JB010451>
- 372 Dill, R., & Dobsław, H. (2013). Numerical simulations of global-scale high-resolution
373 hydrological crustal deformations. *Journal of Geophysical Research: Solid Earth*, 118(9),
374 5008–5017. <https://doi.org/10.1002/jgrb.50353>
- 375 Dziewonski, A. M., & Anderson, D. L. (1981). Preliminary reference Earth model. *Physics of*
376 *the Earth and Planetary Interiors*, 25(4), 297–356. [https://doi.org/10.1016/0031-](https://doi.org/10.1016/0031-9201(81)90046-7)
377 [9201\(81\)90046-7](https://doi.org/10.1016/0031-9201(81)90046-7)
- 378 Farrell, W. E. (1972). Deformation of the Earth by Surface Loads. *REVIEWS OF*
379 *GEOPHYSICS AND SPACE PHYSICS*, 10(3), 761–797.

- 380 Ferreira, V., Ndehedehe, C., Montecino, H., Yong, B., Yuan, P., Abdalla, A., & Mohammed,
381 A. (2019). Prospects for imaging terrestrial water storage in south america using daily
382 GPS observations. *Remote Sensing*, *11*(6), 679. <https://doi.org/10.3390/rs11060679>
- 383 Fu, Y., Argus, D. F., & Landerer, F. W. (2015). GPS as an independent measurement to
384 estimate terrestrial water storage variations in Washington and Oregon. *Journal of*
385 *Geophysical Research: Solid Earth*, *120*(1), 552–566.
386 <https://doi.org/10.1002/2014JB011415>
- 387 Ghorbani, Z., Khosravi, A., Maghsoudi, Y., Mojtahedi, F. F., Javadnia, E., & Nazari, A.
388 (2022). Use of InSAR data for measuring land subsidence induced by groundwater
389 withdrawal and climate change in Ardabil Plain, Iran. *Scientific Reports*, *12*(1), 13998.
390 <https://doi.org/10.1038/s41598-022-17438-y>
- 391 Gualandi, A., Serpelloni, E., & Belardinelli, M. E. (2014). Space-time evolution of crustal
392 deformation related to the Mw 6.3, 2009 L’Aquila earthquake (central Italy) from
393 principal component analysis inversion of GPS position time-series. *Geophysical Journal*
394 *International*, *197*(1), 174–191. <https://doi.org/10.1093/gji/ggt522>
- 395 Gualandi, A., Serpelloni, E., & Belardinelli, M. E. (2016). Blind source separation problem in
396 GPS time series. *Journal of Geodesy*, *90*(4), 323–341. [https://doi.org/10.1007/s00190-](https://doi.org/10.1007/s00190-015-0875-4)
397 [015-0875-4](https://doi.org/10.1007/s00190-015-0875-4)
- 398 He, X., Yu, K., Montillet, J.-P., Xiong, C., Lu, T., Zhou, S., Ma, X., Cui, H., & Ming, F.
399 (2020). GNSS-TS-NRS: An Open-Source MATLAB-Based GNSS Time Series Noise
400 Reduction Software, *Remote Sensing (Basel)*, *12*, 3532.
401 <https://doi.org/10.3390/rs12213532>
- 402 Jiang, Z., Hsu, Y.-J., Yuan, L., & Huang, D. (2021). Monitoring time-varying terrestrial water
403 storage changes using daily GNSS measurements in Yunnan, southwest China. *Remote*
404 *Sensing of Environment*, *254*, 112249. <https://doi.org/10.1016/j.rse.2020.112249>

- 405 Jiang, Z., Hsu, Y.-J., Yuan, L., Feng, W., Yang, X., & Tang, M. (2022). GNSS2TWS: an
406 open-source MATLAB-based tool for inferring daily terrestrial water storage changes
407 using GNSS vertical data. *GPS Solutions*, 26(4), 114. [https://doi.org/10.1007/s10291-022-](https://doi.org/10.1007/s10291-022-01301-8)
408 01301-8
- 409 Jin, S., & Zhang, T. (2016). Terrestrial Water Storage Anomalies Associated with Drought in
410 Southwestern USA from GPS Observations. *Surveys in Geophysics*, 37(6), 1139–1156.
411 <https://doi.org/10.1007/s10712-016-9385-z>
- 412 Knappe, E., Bendick, R., Martens, H. R., Argus, D. F., & Gardner, W. P. (2019). Downscaling
413 vertical GPS observations to derive watershed-scale hydrologic loading in the northern
414 rockies. *Water Resources Research*, 55(1), 391–401.
415 <https://doi.org/10.1029/2018WR023289>
- 416 Kositsky, A. P., & Avouac, J. P. (2010). Inverting geodetic time series with a principal
417 component analysis-based inversion method. *Journal of Geophysical Research*, 115(B3).
418 <https://doi.org/10.1029/2009JB006535>
- 419 Pintori, Francesco; Serpelloni, Enrico (2023): Vertical displacement time series from GNSS
420 stations in the Po river basin area [Dataset]. PANGAEA,
421 <https://doi.pangaea.de/10.1594/PANGAEA.958598>
- 422 Pintori, F., Serpelloni, E., & Gualandi, A. (2022). Common-mode signals and vertical
423 velocities in the greater Alpine area from GNSS data. *Solid Earth*, 13(10), 1541–1567.
424 <https://doi.org/10.5194/se-13-1541-2022>
- 425 Rodell, M., Houser, P. R., Jambor, U., Gottschalck, J., Mitchell, K., Meng, C. J., et al. (2004).
426 The global land data assimilation system. *Bulletin of the American Meteorological*
427 *Society*, 85(3), 381–394. <https://doi.org/10.1175/BAMS-85-3-381>
- 428 Save, H., Bettadpur, S., & Tapley, B. D. (2016). High-resolution CSR GRACE RL06 mascons
429 Version 2. *Journal of Geophysical Research: Solid Earth*, 121(10), 7547–7569.
430 <https://doi.org/10.1002/2016JB013007>

- 431 Save, H. (2020). "CSR GRACE and GRACE-FO RL06 Mascon Solutions v02",
432 <https://doi.org/10.15781/cgq9-nh24>
- 433 Serpelloni, E., Cavaliere, A., Martelli, L., Pintori, F., Anderlini, L., Borghi, A., et al. (2022).
434 Surface Velocities and Strain-Rates in the Euro-Mediterranean Region From Massive
435 GPS Data Processing. *Frontiers in Earth Science*, 10.
436 <https://doi.org/10.3389/feart.2022.907897>
- 437 Sternai, P., Sue, C., Husson, L., Serpelloni, E., Becker, T. W., Willett, S. D., et al. (2019).
438 Present-day uplift of the European Alps: Evaluating mechanisms and models of their
439 relative contributions. *Earth-Science Reviews*, 190, 589–604.
440 <https://doi.org/10.1016/j.earscirev.2019.01.005>
- 441 Toreti, A., Bavera, D., Avanzi, F., Cammalleri, C., De Felice, M., de Jager, A., et al. (2022).
442 Drought in northern Italy March 2022 : GDO analytical report. *Publications Office of the*
443 *European Union*. <https://doi.org/10.2760/781876>
- 444 Wessel, P., Luis, J. F., Uieda, L., Scharoo, R., Wobbe, F., Smith, W. H. F., & Tian, D. (2019).
445 The Generic Mapping Tools version 6. *Geochemistry, Geophysics, Geosystems*, 20(11),
446 5556– 5564. <https://doi.org/10.1029/2019GC008515>
- 447 Vicente-Serrano, S. M., Beguería, S., & López-Moreno, J. I. (2010). A Multiscalar Drought
448 Index Sensitive to Global Warming: The Standardized Precipitation Evapotranspiration
449 Index. *Journal of Climate*, 23(7), 1696–1718. <https://doi.org/10.1175/2009JCLI2909.1>
- 450 White, A. M., Gardner, W. P., Borsa, A. A., Argus, D. F., & Martens, H. R. (2022). A review
451 of GNSS/GPS in hydrogeodesy: hydrologic loading applications and their implications
452 for water resource research. *Water Resources Research*, 58(7), e2022WR032078.
453 <https://doi.org/10.1029/2022WR032078>
- 454 Wu, D., Yan, H., & Yuan, S. (2018). L1 regularization for detecting offsets and trend change
455 points in GNSS time series. *GPS Solutions*, 22(3), 88. [https://doi.org/10.1007/s10291-](https://doi.org/10.1007/s10291-018-0756-4)
456 [018-0756-4](https://doi.org/10.1007/s10291-018-0756-4)

- 457 Zhang, B., Yao, Y., Fok, H. S., Hu, Y., & Chen, Q. (2016). Potential Seasonal Terrestrial
458 Water Storage Monitoring from GPS Vertical Displacements: A Case Study in the Lower
459 Three-Rivers Headwater Region, China. *Sensors (Basel, Switzerland)*, 16(9).
460 <https://doi.org/10.3390/s16091526>
- 461 Zhang, L., Yi, S., Wang, Q., Chang, L., Tang, H., & Sun, W. (2019). Evaluation of GRACE
462 mascon solutions for small spatial scales and localized mass sources. *Geophysical*
463 *Journal International*, 218(2), 1307–1321. <https://doi.org/10.1093/gji/ggz198>

15 **Abstract**

16 We study vertical ground displacement time-series from GNSS stations in the Po river basin to
17 measure deformation signals associated with the severe drought occurring since 2021 and
18 estimate the spatial distribution of water loss. The detection of vertical ground displacement
19 trend changes allows us to extract a spatially correlated signal that follows the Po level trend
20 changes and SPEI-12 drought index. GNSS stations in the basin mostly underwent uplift, up to
21 7 mm, since 2021, which corresponds to ~80 Gtons of water loss. Compared to GLDAS and
22 GRACE, the GNSS results show a similar temporal evolution of water content, but a different
23 spatial distribution. Our study indicates that using dense GNSS networks is an effective way to
24 monitor long-term changes in water storage even in small water basins and serve as a reliable
25 indicator of drought severity.

26 **Plain Language Summary**

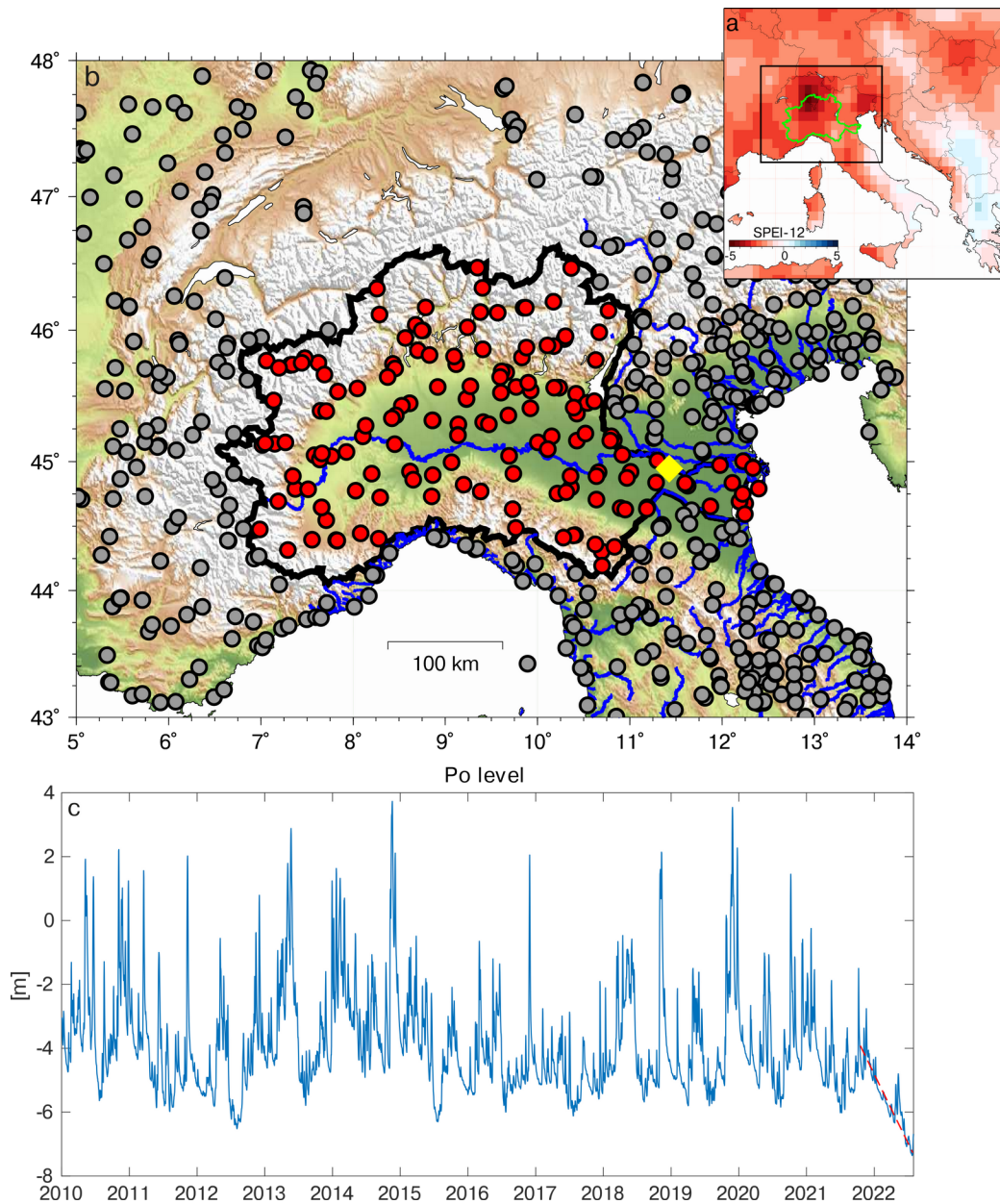
27 This study looks at the way the ground moves up and down in the Po river basin, in northern
28 Italy, using Global Navigation Satellite System (GNSS) stations. We measure how much
29 water was lost during a big drought in the area since 2021. We find that the GNSS stations
30 show that the ground mostly moved upwards since 2021, which means that water was being
31 lost. We estimate that about 80 billion tons was lost during that time, in agreement with other
32 ways of measuring terrestrial water variations. This study shows that GNSS stations can be an
33 alternative way to measure how much water is being lost during drought in small areas and
34 common vertical displacement signals are a good approximation of drought indexes.

35 **1 Introduction**

36 Drought is one of the most complex recurring natural disasters, defined by a deficiency
37 of precipitations that causes prolonged water scarcity. Failure to manage drought risk has the
38 potential to have dire consequences for people, livelihoods, economy and ecosystems. During
39 the summer of 2022 Italy faced a severe drought, where the dry conditions were related to a
40 persistent lack of precipitation since December 2021. The level of the largest Italian river, the
41 Po, has been significantly decreasing since the summer of 2021 (Fig. 1). Several regions
42 declared a state of emergency, and drinking water has been rationed in hundreds of
43 municipalities in northern Italy. Figure 1 shows a map of the Standardised Precipitation-

44 Evapotranspiration Index (SPEI-12, Vicente-Serrano et al. 2010), which quantifies the drought
 45 level of the last 12 months taking into account both precipitation and potential
 46 evapotranspiration.

47



48 **Figure 1. a) SPEI-12 computed on August 2022. b) The study area: the black line**
 49 **represents the Po river (thick blue line) basin; the dots show the positions of the GNSS**
 50 **stations used in the analysis, the reds are the ones inside the basin, the gray the ones**
 51 **outside; the yellow diamond shows the location of the Po level measurement point. c) Po**
 52 **river level changes. The rapid level drop between 2021 and 2022 is shown by the red**
 53 **dashed line.**

54 The effects of droughts are particularly dangerous in the Po river basin for various
55 reasons: drought threatens the crops in the Po Valley, which are around 40% of the total food
56 produced in Italy, and impacts energy production, since a reduced river flow causes
57 deficiencies in hydropower generation and cooling of thermal plants (Boyko et al., 2022).

58 Due to global warming, more frequent and severe droughts are likely to occur in the
59 next future (Boyko et al., 2022). For this reason, while it is necessary to measure and monitor
60 variations in terrestrial water storage (TWS) in order to evaluate the best policies to address
61 the problems caused by water scarcity, it is difficult to get measurements of all the TWS
62 components, which include groundwater, surface water, vegetation and soil moisture, ice and
63 snow. Piezometers, for example, effectively monitor groundwater level variations but not the
64 other water storage components, and evaluating the water volume changes from them is not
65 straightforward. On the other hand, the Global Land Data Assimilation System (GLDAS)
66 model provides daily variations of the soil moisture and snow water equivalent, but it can not
67 take into account the groundwater stored more than 2 m below the surface (Argus et al., 2014;
68 Jiang et al., 2021). TWS can also be estimated using Gravity Recovery and Climate
69 Experiment (GRACE) measurements, which allow modeling water storage changes by
70 inverting the spatiotemporal variations of the Earth's gravity field. Unlike GLDAS, all the
71 components of TWS are taken into account by GRACE, nonetheless its spatial resolution
72 (300-400 km) and its temporal resolution (monthly) are too coarse for many regional or local
73 studies (Fu et al., 2015; Knappe et al., 2019).

74 TWS variations are indirectly detectable not only through gravity data but also by
75 measuring ground displacements through geodetic observations: a water content increase
76 causes an increasing load on the Earth surface, which subsides elastically; while when the
77 water content decreases the crust moves upward because of the water content decrease. Global
78 Navigation Satellite System (GNSS) measurements, for example, provide daily measurements
79 of ground displacements, at mm precisions, that can be used to measure ground deformation
80 associated with TWS variations. Argus et al. (2014) inferred the spatial distribution of the
81 TWS seasonal amplitude, expressed in terms of equivalent water height (EWH), by inverting
82 the seasonal vertical displacements of the ground in California. Fu et al. (2015) estimated
83 TWS variations from GNSS measurements of vertical displacement in Washington and
84 Oregon, finding that the largest seasonal variations of water content were localized in the

85 mountain areas. GNSS displacements have been inverted to estimate the TWS also by Jin and
86 Zhang (2016) in the southwestern United States, by Zhang et al. (2016) over the Yunnan
87 Province in China and by Ferreira et al. (2019) in the entire South America.

88 Carlson et al. (2022) computed TWS in California using a joint inversion method
89 combining the GRACE products with the results of the inversion of GNSS data, taking
90 advantage of the dense spatial distribution of GNSS data together with GRACE's ability to
91 provide regional closure of the water budget.

92 In this work we estimate the amount of water loss in the Po river basin, extending
93 $\sim 7.4 \cdot 10^5$ km², by inverting vertical ground displacements measured by continuous GNSS
94 stations. We consider stations inside the basin, but also stations located within 1° from the
95 basin boundaries, in order to reduce inversion artifacts near the boundaries of the study region
96 (Fu et al. 2015). We focus on long-term, inter-annual, changes, rather than seasonal (i.e.,
97 annual) variations, by modeling displacement time-series looking for trend changes in the
98 vertical component, with particular focus on the most recent and severe 2021-2022 drought.

99 In Section 2 we describe the GNSS data used and the methods applied to analyze the
100 vertical displacement time series; in Section 3 we show the relationship between geodetic and
101 hydrological observations and provide a quantitative estimation of the evolution of the TWS.
102 In Section 4 we discuss the results, in light of alternative estimates of water storage variations.

103 2 Data and Methods

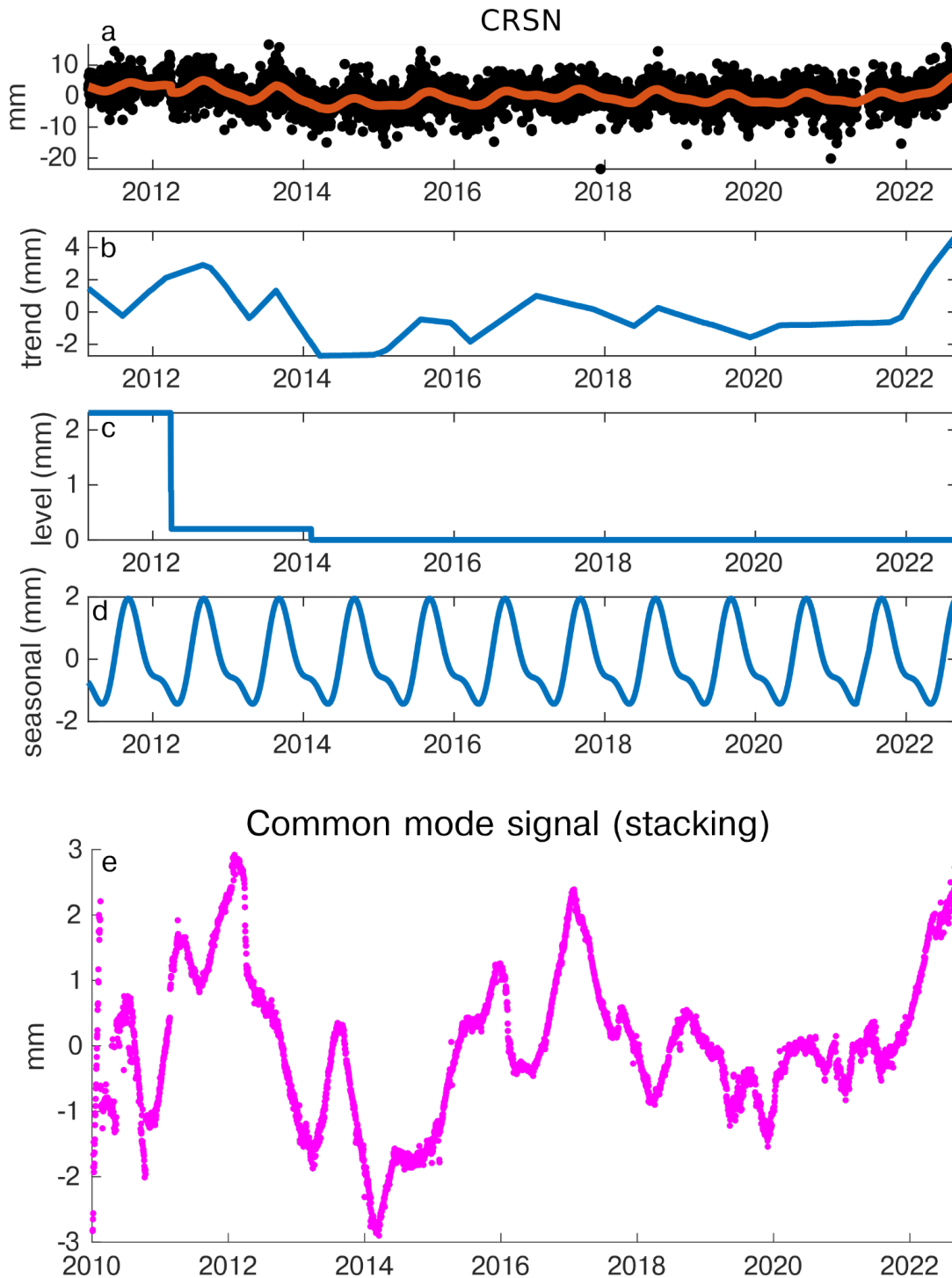
104 We consider ~180 daily GNSS vertical ground displacement time series from January,
 105 2010 to September, 2022 of continuous stations located in the Po river basin (see Fig. 1). We
 106 also include in the analysis ~280 stations located within 1° of the catchment limits. This is part
 107 of a larger geodetic solution encompassing the whole Euro-Mediterranean region, obtained
 108 following the approach detailed in Serpelloni et al. (2022). We remove the long-term linear
 109 trend from the time series using the Median Interannual Difference Adjusted for Skewness
 110 (MIDAS) estimator (Blewitt et al. 2016) and filter the contribution of the non-tidal
 111 atmospheric loading (NTAL), as suggested by White et al. (2022), since they can produce
 112 displacements of several millimeters at daily-weekly timescales that can interfere with the
 113 hydrological signal. The NTAL-induced vertical displacements are evaluated from the daily
 114 0.5° x 0.5° gridded solution of the Earth-System-Modeling Group at the German Research
 115 Center for Geosciences (Dill and Dobsław, 2013) and its contribution in each site is calculated
 116 considering the nearest grid point where the displacements associated with NTAL are
 117 computed.

118 The resulting GNSS vertical displacements time series are then analyzed using a trend
 119 filtering approach, which performs an extensive analysis using a L1 norm regularization
 120 model to identify the seasonal components, offsets and linear trend changepoints in the GNSS
 121 time series (Wu et al. 2018). The piecewise trend x is estimated by minimizing the weighted
 122 sum objective function:

$$123 \quad (1/2)\|y - x - s - w\|_2^2 + \lambda \|D^{(2)}x\|_1 + \rho \|1 + D^{(1)}w\|_1$$

124 where y is the original time series, w indicates the level component associated with the
125 offsets, s is the seasonal term, $\|\cdot\|_1$ represents the L1 norm and $D^{(n)}$ are the n -th difference
126 matrix defined as in Wu et al. (2018). λ and ρ are positive parameters controlling the knots of
127 the estimation trend and the frequency of level shifts, respectively (we choose $\lambda=2000$ and $\rho=$
128 80). Figure 2 shows an example of output of this analysis. Focusing on transients and
129 interannual variations, we only consider the extracted piecewise trends, not the seasonal terms
130 having annual and semi-annual frequencies. For some stations level changes (i.e., offsets) not
131 associated with tectonic events or equipment changes are highlighted, which mostly represent
132 fast variations in ground displacements (see Fig. 2 in 2012). For this reason, in the further
133 steps we consider the piecewise trend as the sum of the trend and level components. As it can
134 be seen in Fig. 2, there is an increase in uplift starting from 2021, which is a common feature
135 in GNSS stations within the Po river basin. Fig. 2e shows the stacking of the vertical
136 piecewise trend time-series for all stations analyzed, which is performed by averaging, for
137 each epoch, the residuals of all the time series resulting by removing the mean and linear trend
138 terms. In order to better characterize the spatial distribution of this deformation signal, we use
139 a multivariate statistical approach, similarly to what is used for tectonic deformation studies
140 (Kositsky and Avouac, 2010; Gualandi et al. 2014).

141



142
 143 **Figure 2. Example of GNSS time series decomposition performed using the L1-norm**
 144 **trend filtering approach. In a) the black dots represent the original time series, the red**
 145 **line the model obtained as the sum of the trend (b), level (c) and seasonal component (d).**
 146 **Panel (e) shows the result of the stacking on the piecewise vertical trends of all the**
 147 **stations inside the Po river basin.**

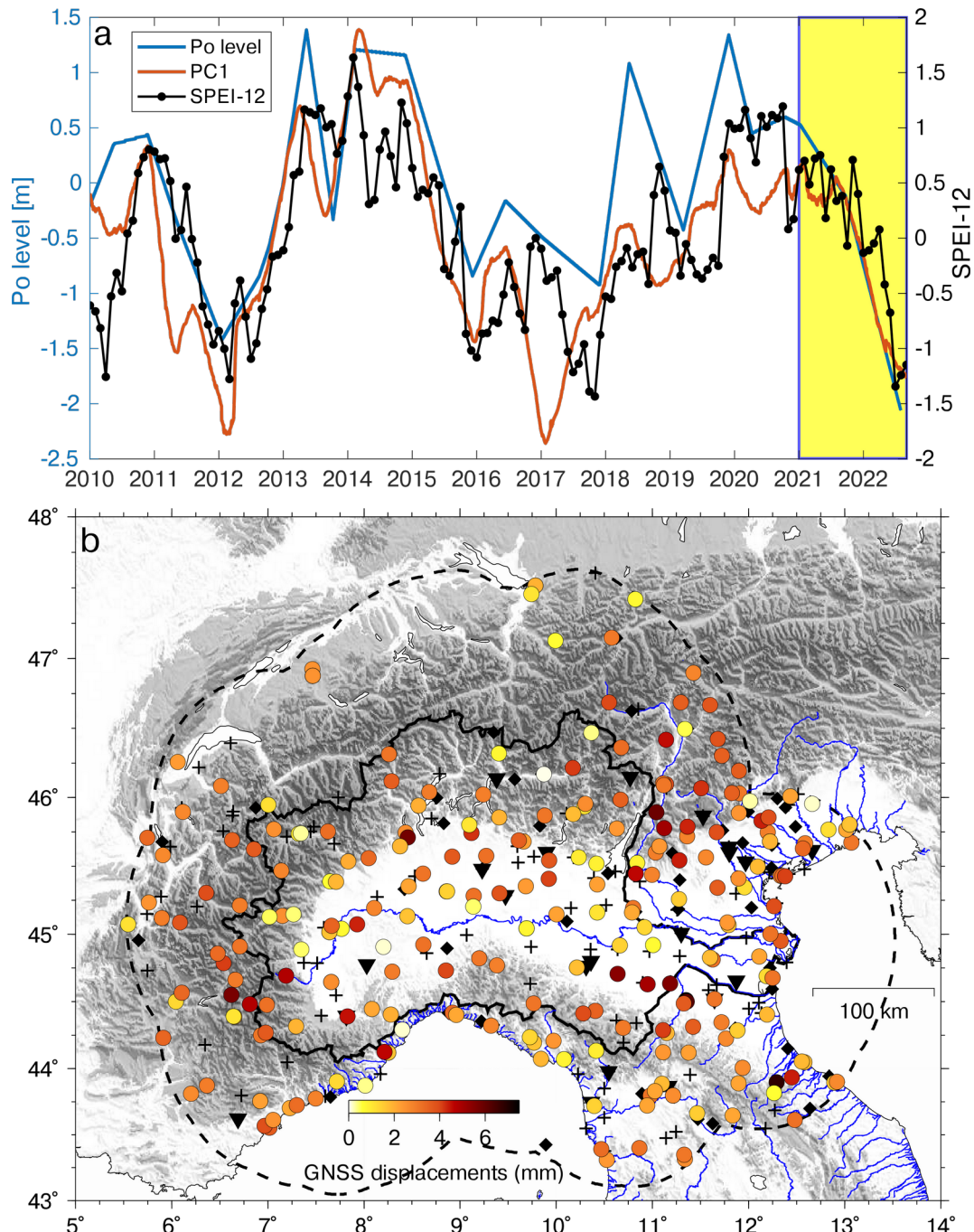
148 **3 Results**

149 3.1 Comparison between geodetic and hydrological measurements

150 We adopt an approach similar to the one described in Jiang et al. (2022), but we use as
151 input of a principal component analysis (PCA) the piecewise vertical trends described in the
152 previous section, rather than the raw time-series. We decompose the dataset using one PC in
153 order to identify the most important common signal of the GNSS stations in the Po basin and
154 retrieve its spatial pattern (i.e., amplitude and sign). However, the first principal component
155 (PC1) obtained performing a PCA using 2 or 3 components is almost identical to the PC1
156 obtained performing a one-component decomposition, both in terms of temporal evolution
157 (Fig. S1) and spatial distributions (Fig. S2).

158 The temporal evolution of PC1 (Fig. 3A) well resembles the common mode signal
159 resulting from a stacking of the vertical trend time-series for all stations (Fig. 2e and Fig. S3).
160 However, the advantage of the PCA is to provide the spatial information on the displacement
161 amplitudes (Fig. S2A).

162 We compare the temporal evolution of PC1 with the SPEI-12 index value, averaged
163 over the Po river basin, and with the Po river level measurements provided by the Regional
164 Agency for Environmental Protection of Veneto region (ARPAV;
165 <https://wwwold.arpa.veneto.it/arpavinforma/bollettini/dati-storici>, Last Access: 20-12-2022).
166 The Po river level time series is filtered adopting the same approach used for the GNSS time-
167 series, and retaining only the piecewise trend component (Fig. S4). On the other hand, SPEI-
168 12 time series does not contain annual variations, since the index is computed as an anomaly
169 over 12 months, then the time series has not been filtered. Figure 3A shows that the geodetic,
170 climatic and hydrological time series are highly temporally correlated.



171 **Figure 3. a) Comparison between the PC1 temporal evolution, the SPEI-12 index and the**
 172 **Po river level. Since PC1 is obtained from detrended GNSS time series, Po river level and**
 173 **SPEI-12 have also been detrended for consistency. b) Vertical displacements associated**
 174 **with PC1 during the 2021.00 (January, 2021) - 2022.67 (September, 2022) time interval**
 175 **(yellow panel). The dashed line represents the boundary of the Po river basin, extended**
 176 **by 1°. Black triangles indicate the 21 stations excluded because they show negative**

177 **displacements; black crosses represent sites with more than 75% of missing data and**
178 **black diamonds the stations with no records after 2021.0.**

179 The vertical displacements associated with PC1 from 2021.00 to 2022.67 are shown in
180 Fig. 3B. Most of the stations show positive values (uplift), in accordance with the hypothesis
181 that in dry periods, when the water load is reduced, the GNSS stations record uplift, while in
182 wet periods the water load increases causing a downward motion of the Earth's surface. We
183 find that this is not true for 21 sites, which show an opposite behavior (black triangles in Fig.
184 3B). Maximum uplift, of the order of 7 mm, is observed in the south-eastern portion of the
185 basin and in the northern portion of the Po basin, which correspond to uplift rates, in the
186 considered two years, that are much faster than the long-term ones (e.g., Pintori et al., 2022).

187 3.2 Inversion of vertical ground displacements

188 The displacements associated with PC1 are inverted using the approach described in
189 Jiang et al. (2022), which estimates water storage variations assuming an elastic response of
190 the Earth to the hydrological load. In order to avoid misinterpretation of the spatial variations
191 of the water storage changes, we exclude from the inversion the 21 stations showing negative
192 vertical displacements (i.e., subsidence, Fig. S5) in the investigated time interval that,
193 following Carlson et al. (2022), are possibly affected by poroelastic processes, causing vertical
194 displacements in the opposite direction compared to the elastic ones. We also exclude from the
195 inversion the GNSS stations that have no observations recorded in the 2021.00-2022.67 time-
196 span (i.e., do not register displacements potentially associated with the last drought episode
197 investigated in this work). The total number of stations used for the inversion is then 250.

198 The relationship between the vertical displacements measured by GNSS x and the
199 water mass load u , expressed as EWH, is

$$200 \quad x = Gu$$

201 where G is the Green's function matrix using load Love numbers of the preliminary reference
 202 earth model (PREM) (Dziewonski and Anderson, 1981) as commonly used in many recent
 203 works (e.g. Carlson et al. 2022, Jiang et al. 2021). The final solution for the daily estimates of
 204 EWH changes u is

$$205 \quad u = (G^T G + \alpha^2 L^T L)^{-1} G^T x$$

206 where L is the Laplacian smoothing matrix and α is the smoothing factor controlling the
 207 relative weight between model roughness and data misfit.

208 We invert the displacements associated with PC1 to estimate EWH on a $0.25^\circ \times 0.25^\circ$
 209 grid. We choose $\alpha = 0.0034$, which is the minimum in the line showing the relation between the
 210 sum of squared residuals from cross-validation (CVSS) and the smoothing factor (Fig. S6),
 211 and use 4 neighbor points for calculating the Laplacian matrix during the least-squares
 212 inversion. Fig. 3A shows the temporal evolution of the EWH averaged over the study area,
 213 while Fig. 3B is a map of the EWH variations that occurred in the 2021.00 - 2022.67 time
 214 interval (yellow box in Fig.3A).

215 Text S1 presents the results of checkerboard tests, showing that our inversion is well
 216 resolved at the spatial resolution of $1^\circ \times 1^\circ$.

217 **4 Discussion**

218 We compare the EWH obtained by inverting the GNSS displacements (EWH_{gnss}) with
 219 surface water content from GLDAS (SWC) and with Liquid Water Equivalent Thickness
 220 (LWE) from GRACE.

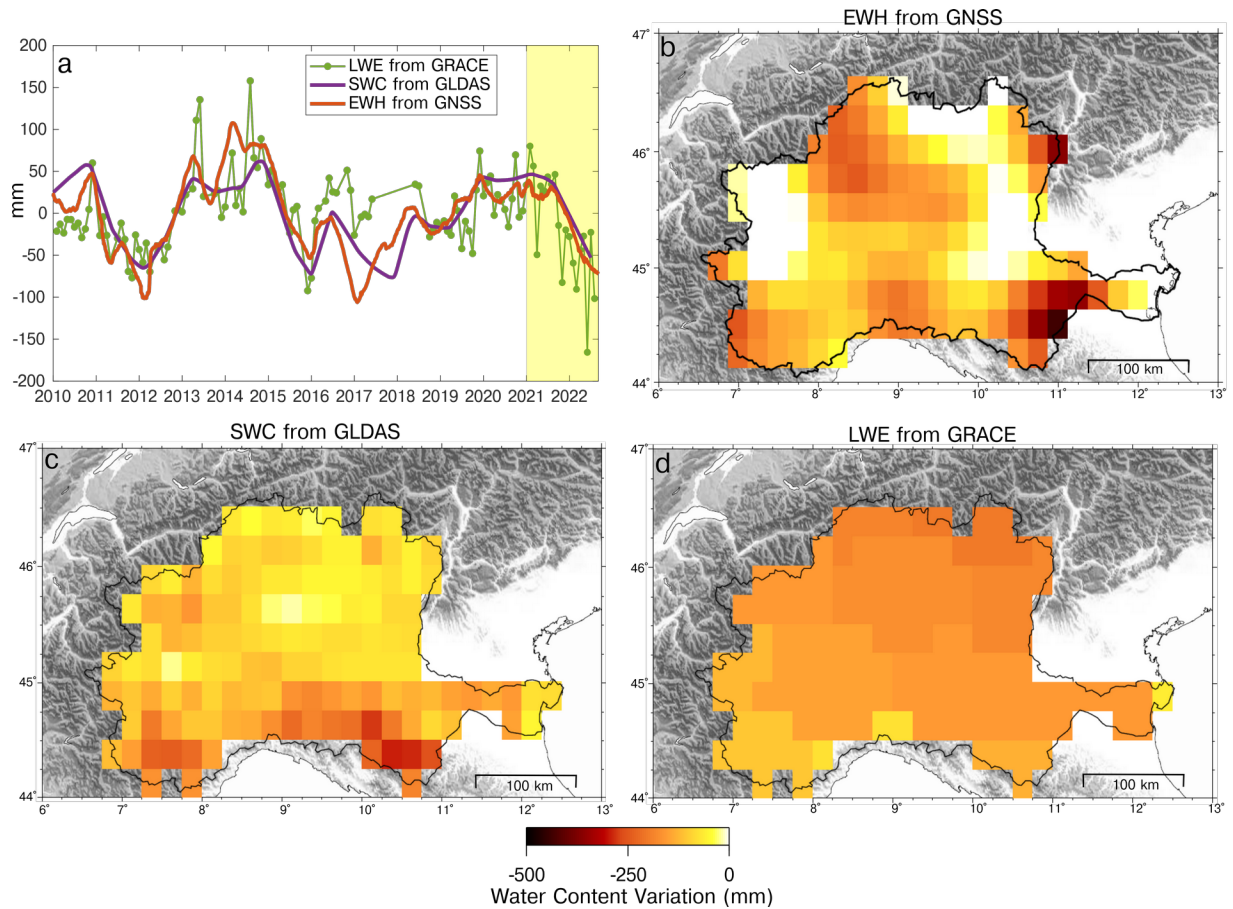
221 The GLDAS products provide the soil moisture content in the first 2 m of the
 222 subsurface, the snow depth water equivalent, the plant canopy surface water and the root zone
 223 soil moisture (Rodell et al., 2004). We consider as SWC the sum of these four components,
 224 which are provided as $0.25^\circ \times 0.25^\circ$ gridded dataset and 3-hours temporal resolution, which are
 225 transformed into daily time series by averaging the 3-hourly time series to make them
 226 consistent with the daily resolution of EWH_{gnss} .

227 LWE is computed using the GRACE and GRACE-FO RL06 Mascon solutions from
228 the Center for Space Research (Save et al., 2016; Save, 2020). While the data are provided in a
229 grid with the same size as the GLDAS one, which corresponds to a resolution of about 25 km,
230 the current resolution is 300-400 km. The temporal resolution of LWE data is monthly and
231 data are missing in correspondence with the gap between the GRACE and GRACE-FO
232 missions, which results in a 11 months gap, from July 2017 to May 2018.

233 The GLDAS products allow an estimate of the water content with a better nominal
234 spatial resolution of $EW_{g_{nss}}$, even though the disadvantage is that GLDAS does not take into
235 account groundwater. Importantly, while the GLDAS nominal spatial resolution is 0.25° , its
236 effective resolution may be different due to the assimilation process and the interpolation
237 techniques used to generate gridded datasets. Furthermore, the nominal spatial resolution of
238 GLDAS may not represent the true spatial variability of soil moisture in a context such as the
239 Po river basin, characterized by high topographic gradients. The correct determination of the
240 soil types in regions characterized by heterogeneous landscapes, elevation and land cover, in
241 fact, is complex and this can lead to errors in soil moisture modeling (Bi et al., 2016).

242 LWE takes into account all TWS components, but with a spatial and temporal
243 resolution much poorer than $EW_{g_{nss}}$. We point out that while $EW_{g_{nss}}$ is inverted on a
244 $0.25^\circ \times 0.25^\circ$ grid, the results of the checkerboard test show that the actual spatial resolution is
245 $\sim 1^\circ$, corresponding to about 100 km (Section S1 of the Supporting Information). This is
246 consistent with the resolution achieved by Zhang et al. (2016) in the Yunnan region of China
247 and by Fu et al. (2015) in Washington and Oregon. The high spatial density of the southern
248 California GNSS network allowed Carlson et al. (2022) to reach a spatial resolution of 80 km,
249 while when considering larger study areas as in Borsa et al. (2014) and in Ferreira et al. (2019)
250 the spatial resolution decreases to 200-300 km.

251 We filter the annual and semiannual signals in SWC time series using the same
252 approach used for GNSS displacement and Po river level measurements (see Fig. S8), and
253 apply a PCA using one PC on the trend components. Because of the monthly temporal
254 resolution of the GRACE products, LWE data are analyzed using a slightly different strategy,
255 removing the annual and semiannual components from the original time series instead of
256 estimating the trend components, as done for GNSS and GLDAS time-series. In fact, the trend
257 variations observed in $EW_{g_{nss}}$ occur also at a monthly timescale, but the temporal resolution
258 of LWE is also monthly, so it is unnecessary to estimate the LWE trend variations. As for the
259 GLDAS and GNSS datasets, the filtered time series are analyzed with a PCA with one PC.
260 Fig. 4a shows the temporal evolutions of the basin-averaged water content expressed as
261 $EW_{g_{nss}}$, SWC from GLDAS and LWE from GRACE, while Fig. 4b-d shows the spatial
262 distributions of water loss from January, 2010 to September, 2022 (yellow box in Fig. 4a),
263 estimated from GNSS, GLDAS and GRACE, respectively.



264 **Figure 4. a) Comparison among the temporal evolutions of the regional-averaged water**
 265 **content expressed as EWH_{gnss} (red), SWC (purple) and LWE (green). Since EWH is**
 266 **obtained from GNSS detrended data; both GLDAS and GRACE data have also been**
 267 **detrended for consistency. b) Water loss occurred in the 2021.00 - 2022.67 time interval**
 268 **in terms of EWH from GNSS, c) SWC from GLDAS and d) LWE from GRACE.**

269 The temporal evolution of the basin-averaged water content estimated by the three
 270 models is very similar, especially between EWH_{gnss} and SWC (Fig. 4a), suggesting that the
 271 water storage variations may be dominated by its superficial content, captured by GLDAS.
 272 The spatial distribution of the water loss occurring in the 2021.00 - 2022.67 time interval (Fig.
 273 4b-d) is different depending on the considered dataset; nonetheless, averaging on the Po basin
 274 surface, we obtain water loss values of the order of about 80, 82 and 115 Gtons from GNSS,
 275 GLDAS and GRACE, respectively in this period.

276 The poor spatial resolution of GRACE measurements makes LWE spatial distribution
277 “smoother” than the other two datasets and not able to detect concentrations of water loss at
278 the scale of the Po river basin. Both SWC and EWH_{gnss} show the largest values in the southern
279 portion of the basin, but EWH_{gnss} is large also in the north-central portion of the basin, in
280 agreement with the SPEI-12 map (Fig. 1), and very small in the eastern and western portions.
281 The reason for the observed spatial discrepancy can be a consequence of the GLDAS
282 limitations in resolving the spatial distribution of the water loss in the mountain sectors. It is
283 also worth considering that GNSS vertical displacements can contain signals that might cause
284 an incorrect estimation of the water content. In fact, the inversion is made on the
285 displacements reconstructed by the PC1. This statistical approach allows us to identify a
286 common displacement signal that has the same temporal evolution in all the GNSS stations,
287 but different amplitudes. The amplitude associated with this signal might be imprecise,
288 especially in GNSS sites characterized by noisy time-series or for stations affected by local
289 processes.

290 Importantly, estimates of water loss values depend on the Green’s function used to
291 invert the displacements data. Several authors (e.g., Argus et al., 2017; Chanard et al., 2014),
292 point out that a gravitating, spherical Earth model is preferred in this context, since non
293 gravitating, half-space models, can understate elastic vertical displacements up to a factor of
294 2.5. Moreover, the results are not very sensitive to the Earth's structure: assuming two
295 different models for the Earth, PREM and the Gutenberg Bullen A Earth structure (Farrell,
296 1972), Argus et al. (2017) find that the difference between the displacements caused by a 450
297 $\text{km} \times 60 \text{ km}$ load is only 4%.

298 **5 Conclusions**

299 We analyze vertical ground displacements from GNSS stations located in the Po river
300 basin, a significant European district with industrial and agricultural settlements. Our study
301 demonstrates that changes in vertical trends respond to meteo-climatic forcing and serve as a
302 reliable, near real-time, independent approximation of drought indexes. During the drought
303 that has affected the region since 2021, we observe a regional uplift signal. This uplift reaches
304 values of up to 7 mm and exhibits spatial variations across the area. We interpret this
305 phenomenon as a result of variable water loss and subsequent reduced load, enabling us to
306 estimate the spatial distribution of EWH. GNSS observations indicate that an estimated
307 average of approximately 80 Gtons of water was lost in the Po river basin from 2021 to the
308 end of summer 2022. This estimate aligns with values obtained from GLDAS but is lower than
309 the estimate derived from GRACE. Additionally, while the temporal evolution of EWH
310 estimated by GNSS, GLDAS, and GRACE shows similarities, the spatial patterns differ
311 significantly.

312 Our findings are also relevant for studying active tectonics and geodynamics. The
313 Apennines and Alps, in fact, exhibit long-term uplift signals resulting from various multiscale
314 processes (Sternai et al., 2019). Accounting for the hydrological origins of trend variations is
315 crucial to improve accuracy and prevent misinterpretation of transient signals or biases in
316 velocity estimates, especially in case of short time-series.

317 Future research will integrate GNSS with InSAR data to improve the spatial resolution
318 of EWH to a few tens of meters, as demonstrated by Ghorbani et al. (2022). This integration
319 would enhance our understanding of the phenomenon and provide more detailed information
320 on water loss and recharge dynamics.

321 **Acknowledgments**

322 We thank GNSS data providers (see Serpelloni et al. 2022 for references), and in
323 particular private networks providers. This study has been partially developed in the
324 framework of the “CLYPEA-Innovation Network for Future Energy” framework, “subsoil
325 deformations” project, funded by the Italian Ecologic Transition Ministry (MITE). Some of

326 the figures are created using the Generic Mapping Tools (GMT) software (Wessel et al.,
327 2013).

328 **Open Research**

329 The EWH is estimated by inverting the GNSS data using the GNSS2TWS software
330 (<https://github.com/jzshhh/gnss2tws>).

331 The trend filtering on the GNSS vertical displacements time series is performed using
332 the L1tool software (<https://github.com/wudingcheng/l1tool>).

333 The stacking of the GNSS time series is performed using the GNSS_TS_NRS code
334 (<https://github.com/CL-Xiong/GNSS-TS-NRS>, He et al., 2020).

335 GLDAS data was downloaded from
336 https://disc.gsfc.nasa.gov/datasets/GLDAS_NOAH025_3H_2.1/summary?keywords=GLDAS.

337 GRACE data was downloaded from <http://www2.csr.utexas.edu/grace>.

338 SPEI-12 data was downloaded from
339 <https://spei.csic.es/map/maps.html#months=1#month=0#year=2023GNSS>.

340 GNSS time series data are available from
341 <https://doi.pangaea.de/10.1594/PANGAEA.958598>.

342 The maps have been made using the GMT software (Wessel et al. 2019).

343 **References**

344 Argus, D. F., Fu, Y., & Landerer, F. W. (2014). Seasonal variation in total water storage in
345 California inferred from GPS observations of vertical land motion. *Geophysical Research*
346 *Letters*, 41(6), 1971–1980. <https://doi.org/10.1002/2014GL059570>

347 Argus, D. F., Landerer, F. W., Wiese, D. N., Martens, H. R., Fu, Y., Famiglietti, J. S., et al.
348 (2017). Sustained water loss in California's mountain ranges during severe drought from
349 2012 to 2015 inferred from GPS. *Journal of Geophysical Research: Solid Earth*, 122(12),
350 10,559-10,585. <https://doi.org/10.1002/2017JB014424>

351 Beaudoin, H. & Rodell, M. NASA/GSFC/HSL (2020), GLDAS Noah Land Surface Model
352 L4 3 hourly 0.25 x 0.25 degree V2.1, Greenbelt, Maryland, USA, Goddard Earth Sciences
353 Data and Information Services Center (GES DISC), Accessed: [10/10/2022],
354 <https://doi.org/10.5067/E7TYRXPJKWOQ>

- 355 Bi, H., Ma, J., Zheng, W., & Zeng, J. (2016). Comparison of soil moisture in GLDAS model
356 simulations and in situ observations over the Tibetan Plateau. *Journal of Geophysical*
357 *Research: Atmospheres*, 121(6), 2658–2678. <https://doi.org/10.1002/2015jd024131>
- 358 Blewitt, G., Kreemer, C., Hammond, W. C., & Gazeaux, J. (2016). MIDAS robust trend
359 estimator for accurate GPS station velocities without step detection. *Journal of*
360 *Geophysical Research. Solid Earth*, 121(3), 2054–2068.
361 <https://doi.org/10.1002/2015JB012552>
- 362 Boyko, O., Reggiani, P., & Todini, E. (2022). Post-processing climate projections of
363 precipitation for the Po river basin: will Italy's North become water-constrained?
364 *Hydrology Research*, 53(11), 1414–1427. <https://doi.org/10.2166/nh.2022.063>
- 365 Carlson, G., Werth, S., & Shirzaei, M. (2022). Joint inversion of GNSS and GRACE for
366 terrestrial water storage change in california. *Journal of Geophysical Research. Solid*
367 *Earth*, 127(3), e2021JB023135. <https://doi.org/10.1029/2021JB023135>
- 368 Chanard, K., Avouac, J. P., Ramillien, G., & Genrich, J. (2014). Modeling deformation
369 induced by seasonal variations of continental water in the Himalaya region: Sensitivity to
370 Earth elastic structure. *Journal of Geophysical Research: Solid Earth*, 119(6), 5097–
371 5113. <https://doi.org/10.1002/2013JB010451>
- 372 Dill, R., & Dobslaw, H. (2013). Numerical simulations of global-scale high-resolution
373 hydrological crustal deformations. *Journal of Geophysical Research: Solid Earth*, 118(9),
374 5008–5017. <https://doi.org/10.1002/jgrb.50353>
- 375 Dziewonski, A. M., & Anderson, D. L. (1981). Preliminary reference Earth model. *Physics of*
376 *the Earth and Planetary Interiors*, 25(4), 297–356. [https://doi.org/10.1016/0031-](https://doi.org/10.1016/0031-9201(81)90046-7)
377 [9201\(81\)90046-7](https://doi.org/10.1016/0031-9201(81)90046-7)
- 378 Farrell, W. E. (1972). Deformation of the Earth by Surface Loads. *REVIEWS OF*
379 *GEOPHYSICS AND SPACE PHYSICS*, 10(3), 761–797.

- 380 Ferreira, V., Ndehedehe, C., Montecino, H., Yong, B., Yuan, P., Abdalla, A., & Mohammed,
381 A. (2019). Prospects for imaging terrestrial water storage in south america using daily
382 GPS observations. *Remote Sensing*, *11*(6), 679. <https://doi.org/10.3390/rs11060679>
- 383 Fu, Y., Argus, D. F., & Landerer, F. W. (2015). GPS as an independent measurement to
384 estimate terrestrial water storage variations in Washington and Oregon. *Journal of*
385 *Geophysical Research: Solid Earth*, *120*(1), 552–566.
386 <https://doi.org/10.1002/2014JB011415>
- 387 Ghorbani, Z., Khosravi, A., Maghsoudi, Y., Mojtahedi, F. F., Javadnia, E., & Nazari, A.
388 (2022). Use of InSAR data for measuring land subsidence induced by groundwater
389 withdrawal and climate change in Ardabil Plain, Iran. *Scientific Reports*, *12*(1), 13998.
390 <https://doi.org/10.1038/s41598-022-17438-y>
- 391 Gualandi, A., Serpelloni, E., & Belardinelli, M. E. (2014). Space-time evolution of crustal
392 deformation related to the Mw 6.3, 2009 L’Aquila earthquake (central Italy) from
393 principal component analysis inversion of GPS position time-series. *Geophysical Journal*
394 *International*, *197*(1), 174–191. <https://doi.org/10.1093/gji/ggt522>
- 395 Gualandi, A., Serpelloni, E., & Belardinelli, M. E. (2016). Blind source separation problem in
396 GPS time series. *Journal of Geodesy*, *90*(4), 323–341. [https://doi.org/10.1007/s00190-](https://doi.org/10.1007/s00190-015-0875-4)
397 [015-0875-4](https://doi.org/10.1007/s00190-015-0875-4)
- 398 He, X., Yu, K., Montillet, J.-P., Xiong, C., Lu, T., Zhou, S., Ma, X., Cui, H., & Ming, F.
399 (2020). GNSS-TS-NRS: An Open-Source MATLAB-Based GNSS Time Series Noise
400 Reduction Software, *Remote Sensing (Basel)*, *12*, 3532.
401 <https://doi.org/10.3390/rs12213532>
- 402 Jiang, Z., Hsu, Y.-J., Yuan, L., & Huang, D. (2021). Monitoring time-varying terrestrial water
403 storage changes using daily GNSS measurements in Yunnan, southwest China. *Remote*
404 *Sensing of Environment*, *254*, 112249. <https://doi.org/10.1016/j.rse.2020.112249>

- 405 Jiang, Z., Hsu, Y.-J., Yuan, L., Feng, W., Yang, X., & Tang, M. (2022). GNSS2TWS: an
406 open-source MATLAB-based tool for inferring daily terrestrial water storage changes
407 using GNSS vertical data. *GPS Solutions*, 26(4), 114. [https://doi.org/10.1007/s10291-022-](https://doi.org/10.1007/s10291-022-01301-8)
408 01301-8
- 409 Jin, S., & Zhang, T. (2016). Terrestrial Water Storage Anomalies Associated with Drought in
410 Southwestern USA from GPS Observations. *Surveys in Geophysics*, 37(6), 1139–1156.
411 <https://doi.org/10.1007/s10712-016-9385-z>
- 412 Knappe, E., Bendick, R., Martens, H. R., Argus, D. F., & Gardner, W. P. (2019). Downscaling
413 vertical GPS observations to derive watershed-scale hydrologic loading in the northern
414 rockies. *Water Resources Research*, 55(1), 391–401.
415 <https://doi.org/10.1029/2018WR023289>
- 416 Kositsky, A. P., & Avouac, J. P. (2010). Inverting geodetic time series with a principal
417 component analysis-based inversion method. *Journal of Geophysical Research*, 115(B3).
418 <https://doi.org/10.1029/2009JB006535>
- 419 Pintori, Francesco; Serpelloni, Enrico (2023): Vertical displacement time series from GNSS
420 stations in the Po river basin area [Dataset]. PANGAEA,
421 <https://doi.pangaea.de/10.1594/PANGAEA.958598>
- 422 Pintori, F., Serpelloni, E., & Gualandi, A. (2022). Common-mode signals and vertical
423 velocities in the greater Alpine area from GNSS data. *Solid Earth*, 13(10), 1541–1567.
424 <https://doi.org/10.5194/se-13-1541-2022>
- 425 Rodell, M., Houser, P. R., Jambor, U., Gottschalck, J., Mitchell, K., Meng, C. J., et al. (2004).
426 The global land data assimilation system. *Bulletin of the American Meteorological*
427 *Society*, 85(3), 381–394. <https://doi.org/10.1175/BAMS-85-3-381>
- 428 Save, H., Bettadpur, S., & Tapley, B. D. (2016). High-resolution CSR GRACE RL06 mascons
429 Version 2. *Journal of Geophysical Research: Solid Earth*, 121(10), 7547–7569.
430 <https://doi.org/10.1002/2016JB013007>

- 431 Save, H. (2020). "CSR GRACE and GRACE-FO RL06 Mascon Solutions v02",
432 <https://doi.org/10.15781/cgq9-nh24>
- 433 Serpelloni, E., Cavaliere, A., Martelli, L., Pintori, F., Anderlini, L., Borghi, A., et al. (2022).
434 Surface Velocities and Strain-Rates in the Euro-Mediterranean Region From Massive
435 GPS Data Processing. *Frontiers in Earth Science*, 10.
436 <https://doi.org/10.3389/feart.2022.907897>
- 437 Sternai, P., Sue, C., Husson, L., Serpelloni, E., Becker, T. W., Willett, S. D., et al. (2019).
438 Present-day uplift of the European Alps: Evaluating mechanisms and models of their
439 relative contributions. *Earth-Science Reviews*, 190, 589–604.
440 <https://doi.org/10.1016/j.earscirev.2019.01.005>
- 441 Toreti, A., Bavera, D., Avanzi, F., Cammalleri, C., De Felice, M., de Jager, A., et al. (2022).
442 Drought in northern Italy March 2022 : GDO analytical report. *Publications Office of the*
443 *European Union*. <https://doi.org/10.2760/781876>
- 444 Wessel, P., Luis, J. F., Uieda, L., Scharoo, R., Wobbe, F., Smith, W. H. F., & Tian, D. (2019).
445 The Generic Mapping Tools version 6. *Geochemistry, Geophysics, Geosystems*, 20(11),
446 5556– 5564. <https://doi.org/10.1029/2019GC008515>
- 447 Vicente-Serrano, S. M., Beguería, S., & López-Moreno, J. I. (2010). A Multiscalar Drought
448 Index Sensitive to Global Warming: The Standardized Precipitation Evapotranspiration
449 Index. *Journal of Climate*, 23(7), 1696–1718. <https://doi.org/10.1175/2009JCLI2909.1>
- 450 White, A. M., Gardner, W. P., Borsa, A. A., Argus, D. F., & Martens, H. R. (2022). A review
451 of GNSS/GPS in hydrogeodesy: hydrologic loading applications and their implications
452 for water resource research. *Water Resources Research*, 58(7), e2022WR032078.
453 <https://doi.org/10.1029/2022WR032078>
- 454 Wu, D., Yan, H., & Yuan, S. (2018). L1 regularization for detecting offsets and trend change
455 points in GNSS time series. *GPS Solutions*, 22(3), 88. [https://doi.org/10.1007/s10291-](https://doi.org/10.1007/s10291-018-0756-4)
456 [018-0756-4](https://doi.org/10.1007/s10291-018-0756-4)

- 457 Zhang, B., Yao, Y., Fok, H. S., Hu, Y., & Chen, Q. (2016). Potential Seasonal Terrestrial
458 Water Storage Monitoring from GPS Vertical Displacements: A Case Study in the Lower
459 Three-Rivers Headwater Region, China. *Sensors (Basel, Switzerland)*, 16(9).
460 <https://doi.org/10.3390/s16091526>
- 461 Zhang, L., Yi, S., Wang, Q., Chang, L., Tang, H., & Sun, W. (2019). Evaluation of GRACE
462 mascon solutions for small spatial scales and localized mass sources. *Geophysical*
463 *Journal International*, 218(2), 1307–1321. <https://doi.org/10.1093/gji/ggz198>



Geophysical Research Letters

Supporting Information for

Drought-induced vertical displacements and water loss in the Po river basin (Northern Italy) from GNSS measurements

F. Pintori¹ and E. Serpelloni¹

¹Istituto Nazionale di Geofisica e Vulcanologia (INGV), Bologna, 40128, Italy.

Contents of this file

Text S1
Figures S1 to S9

Introduction

We provide additional figures to better explain how the time series are analyzed. These figures also support the inversion strategy employed to estimate the terrestrial water storage variations and what is presented in the discussion. Furthermore, Text S1 provides a detailed description of the checkerboard tests used to determine the spatial resolution of the terrestrial water storage variations.

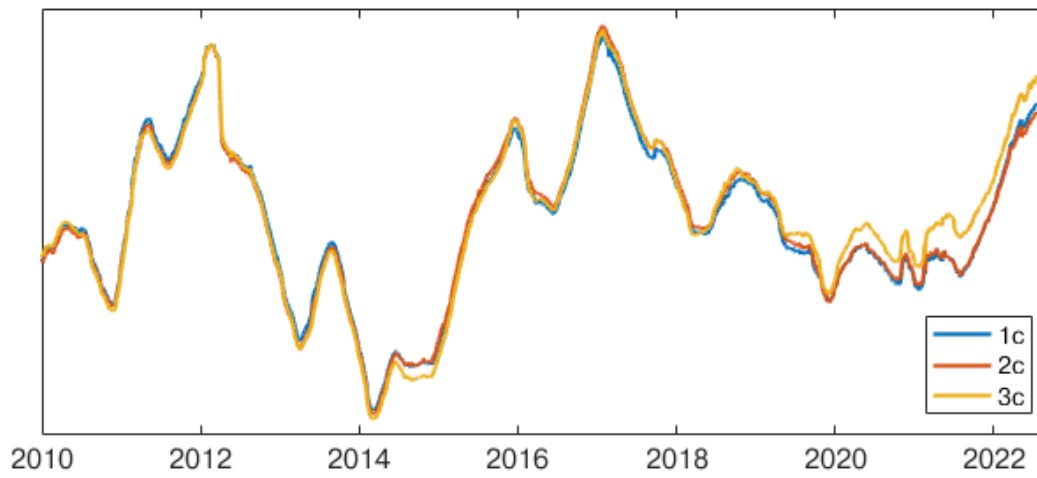


Figure S1. Comparison of the temporal evolution of the PC1 obtained considering 1 (blue), 2 (red) and 3 (yellow) total principal components.

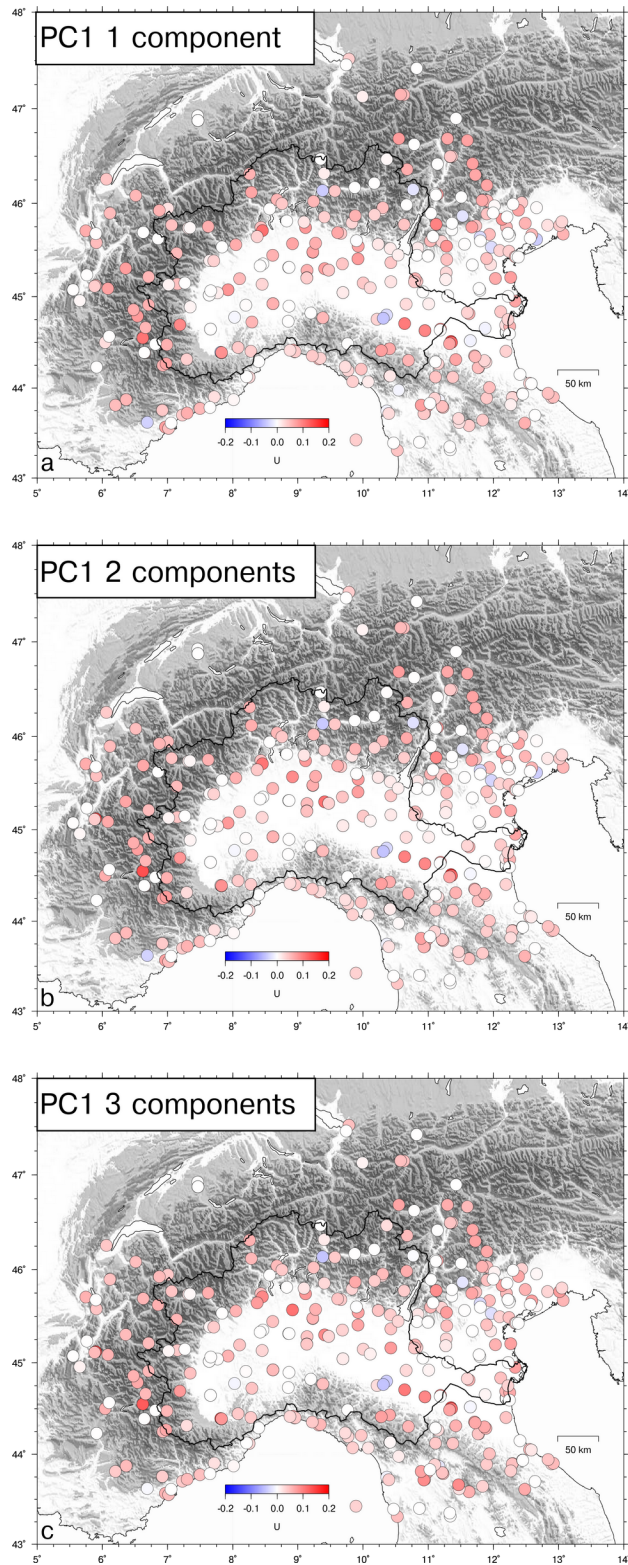


Figure S2. Comparison of the spatial responses of the PC1 obtained considering 1 (a), 2 (b) and 3 (c) total principal components.

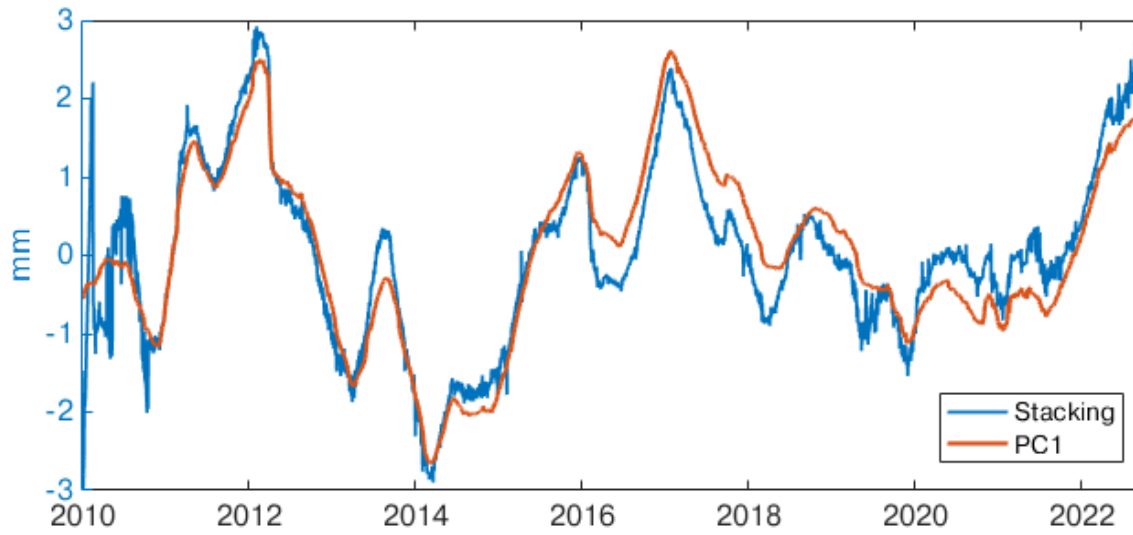


Figure S3. Comparison of the temporal evolution of the PC1 (red) with the common mode signal of the network obtained by performing a weighted stacking (blue).

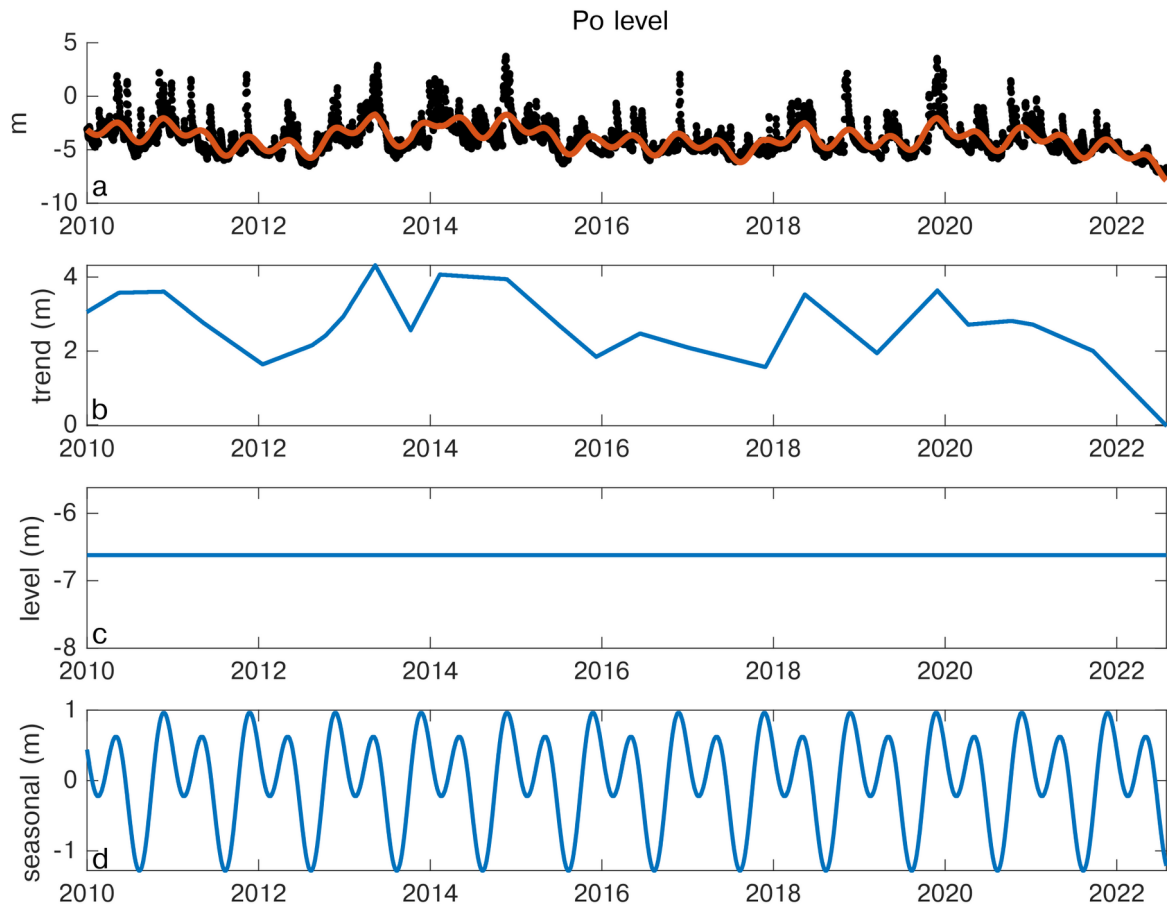


Figure S4. Decomposition of the Po river level measurements, performed using the L1 tool software. In a) the black dots represent the original time series, the red line the L1 tool model, which is the sum of the trend (b), level (c) and seasonal component (d).

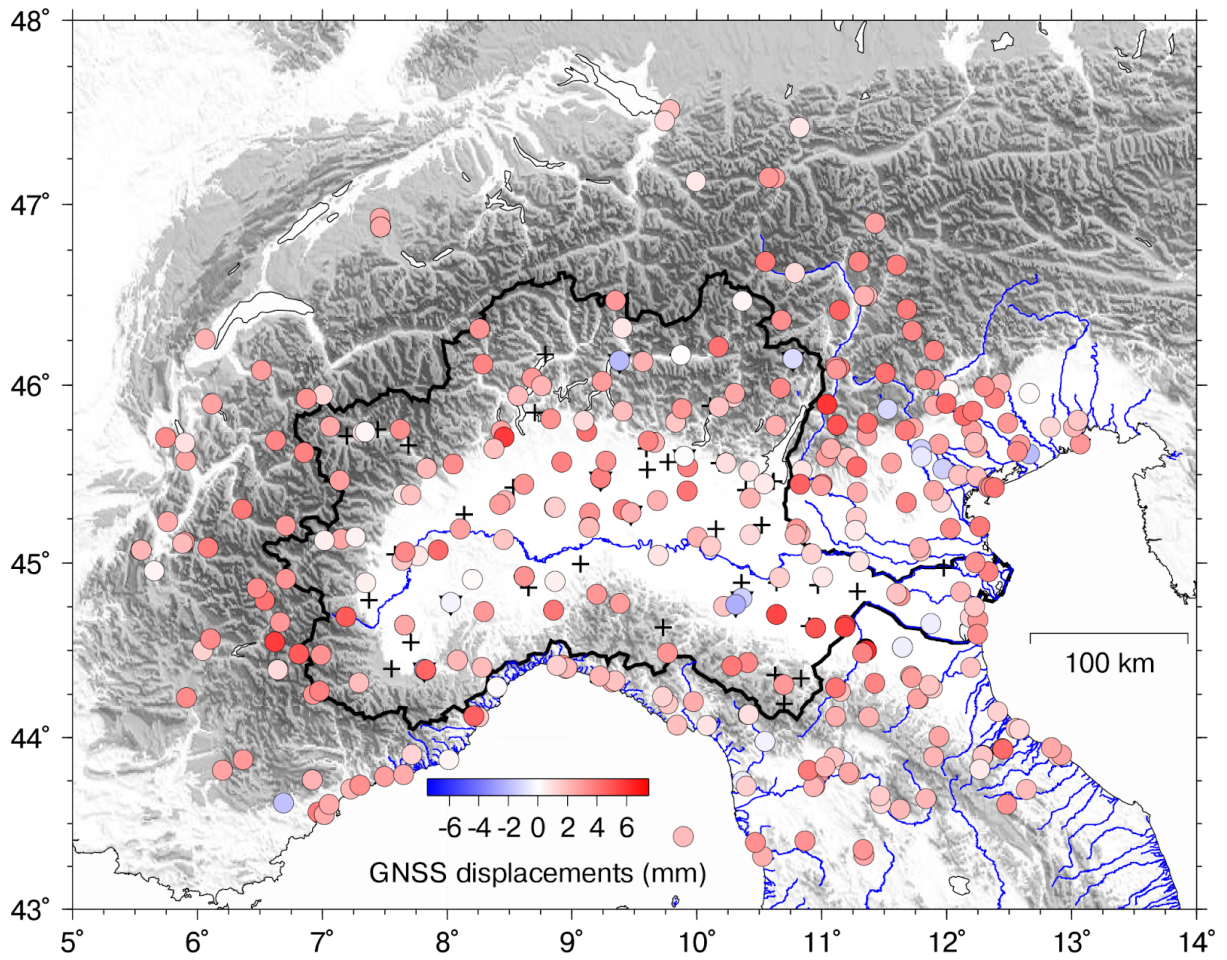


Figure S5. Vertical displacements associated with PC1 during the 2021.00 (January, 2021) - 2022.67 (September, 2022) time interval.

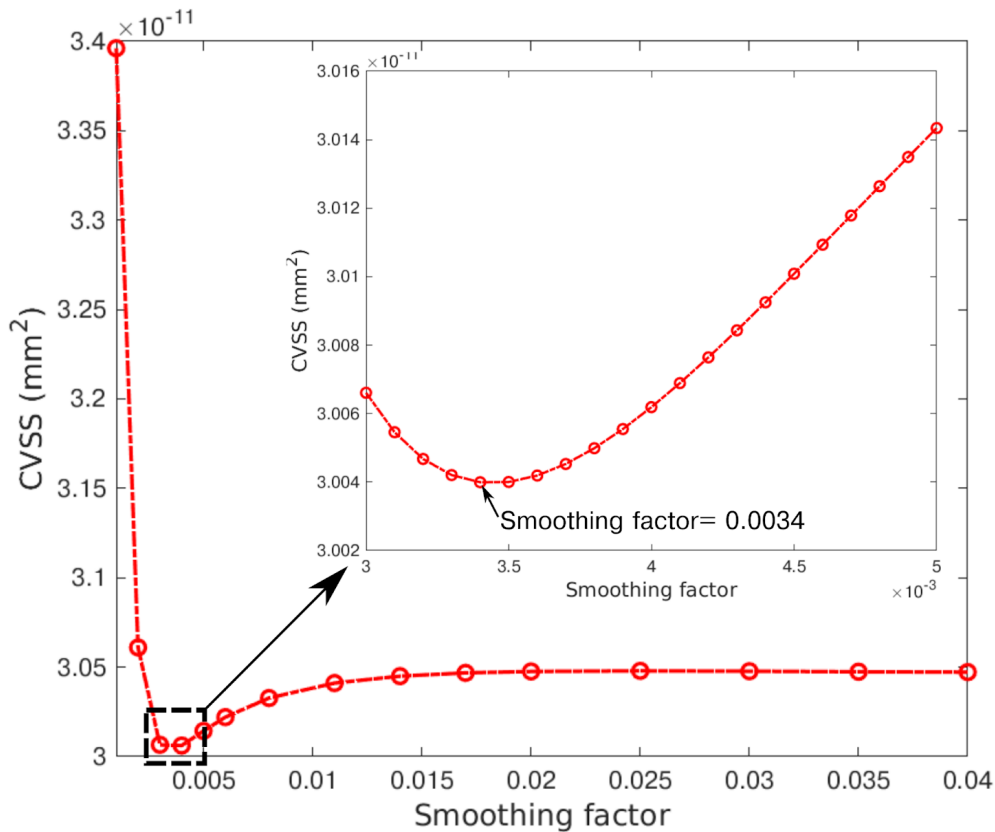


Figure S6. Relation between the sum of squared residuals from cross-validation (CVSS) and the smoothing factor.

Text S1.

A checkerboard test using synthetic inputs is performed to show the ability of the inversion method and the distribution of the GNSS stations to resolve spatial features of water mass variation in a checkerboard pattern, where each mass has dimensions of $1^\circ \times 1^\circ$ and an EWH change of 300 mm (Fig. S7a). The inversion performance is evaluated estimating the agreement dR between each grid point of the checkerboard synthetic model within the Po river basin and the results of the inversion (Fig. S7a) using the following equation, which estimates the percentage of accuracy:

$$dR = 1 - \frac{|input - output|}{\max(input)}$$

where *input* is the value of the checkerboard synthetic model, *output* the value resulting from the inversion and $\max(input)$ the maximum value of *input*, i.e. 300 mm.

The mean value of dR computed over all the grid points is 0.67, then we can conclude that the accuracy of our inversion, at the resolution of $1^\circ \times 1^\circ$, is 67%. By using smaller patches we find a rapid degradation of the spatial accuracy (Fig. S7a-b).

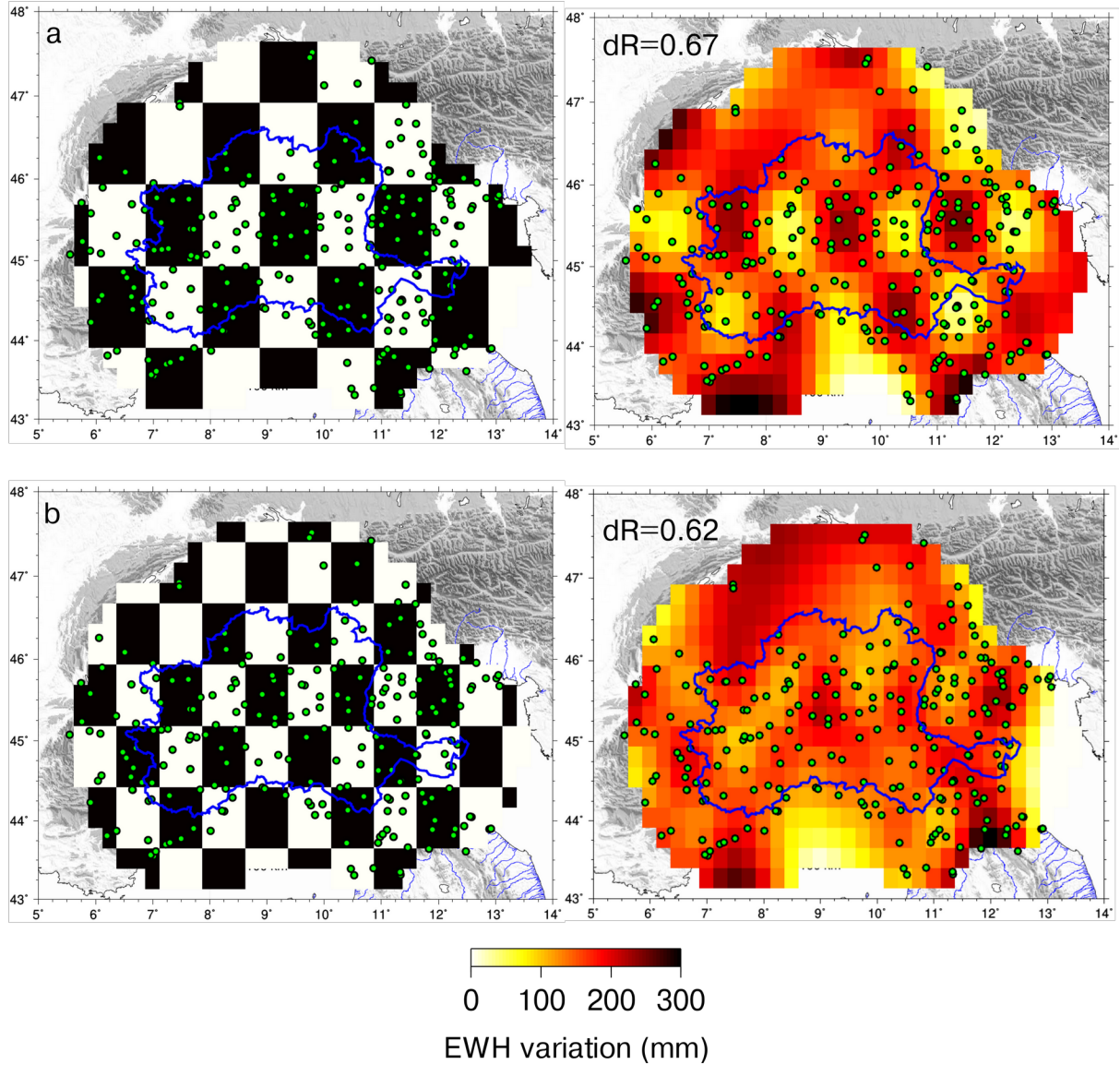


Figure S7. Checkerboard test using synthetic data. a) Comparison between the checkerboard synthetic model (left) and the results using the GNSS2TWS inversion method (right) considering a 1.00° spatial resolution. b) Same as a) but considering a 0.75° spatial resolution.

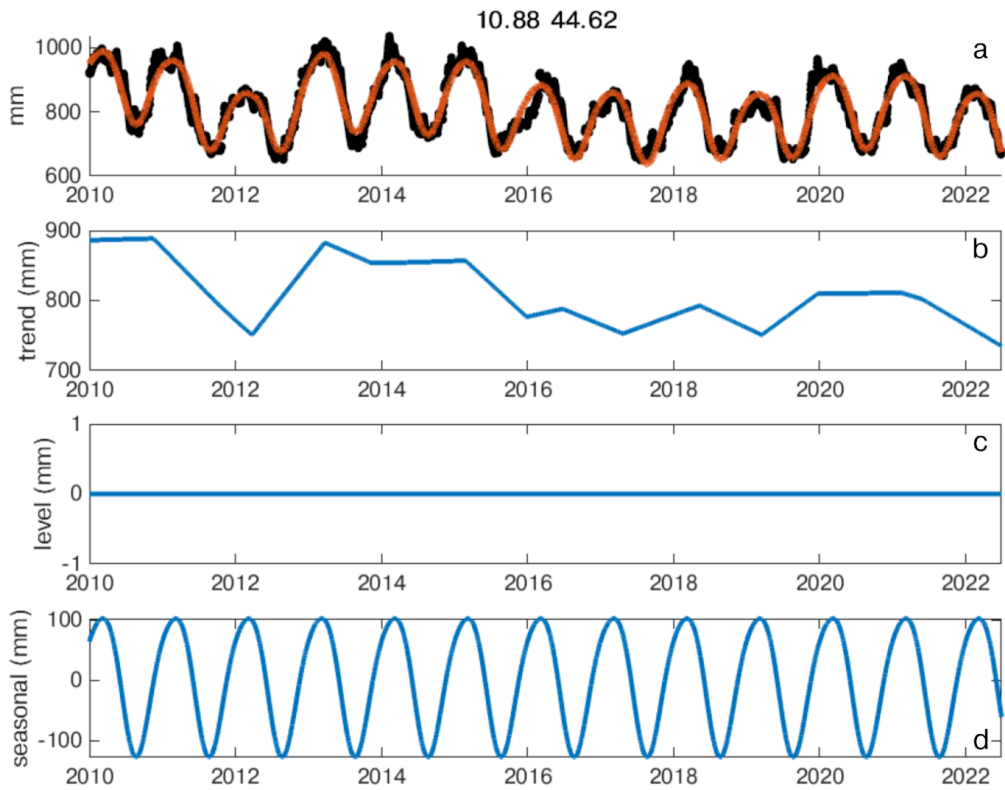


Figure S8. Decomposition of the GLDAS surface water content time series, associated with the cell with coordinates lon= 10.88°, lat= 44.62°, performed using the L1 tool software. In a) the black dots represent the original time series, the red line the L1 tool model, which is the sum of the trend (b), level (c) and seasonal component (d).

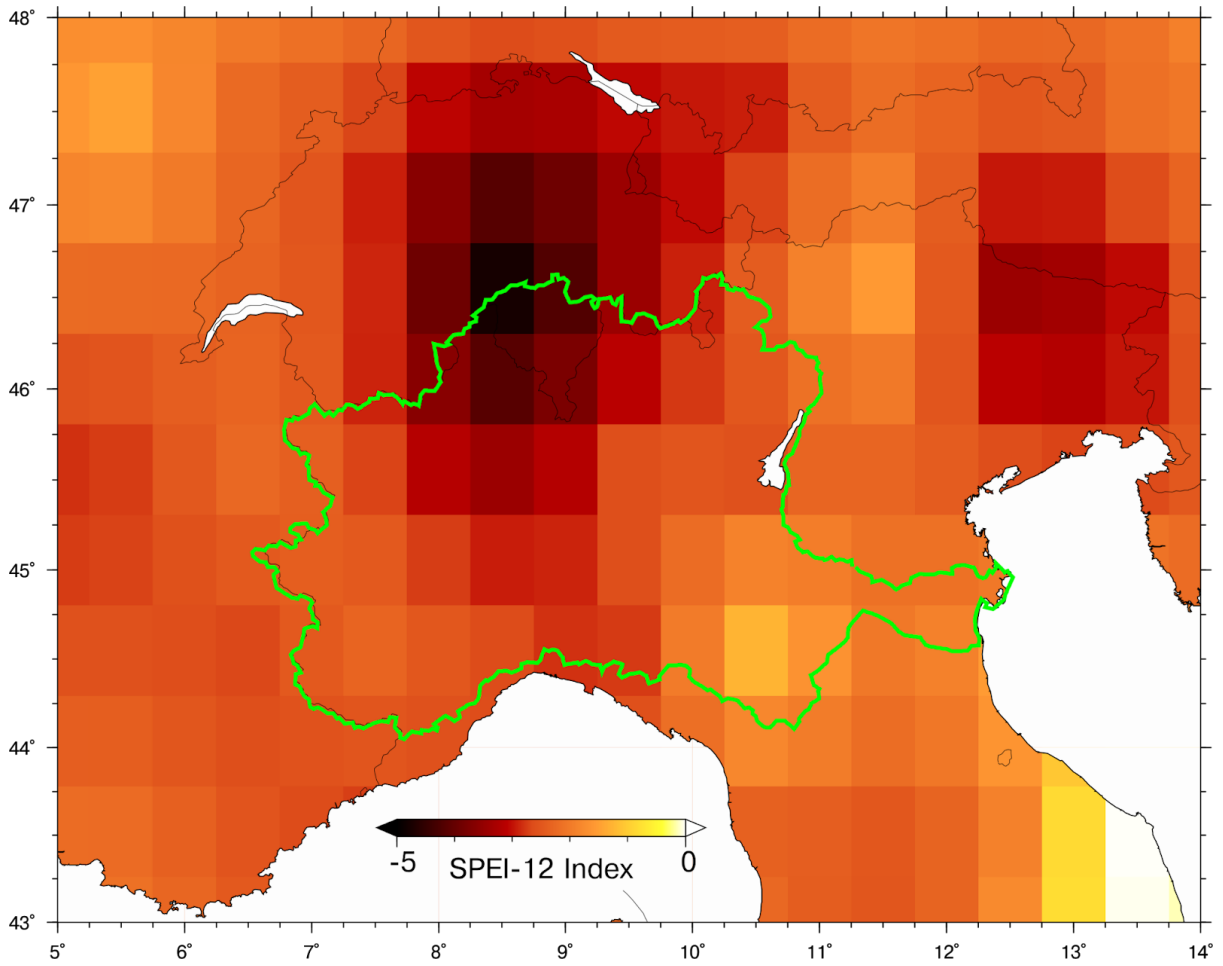


Figure S9. Zoom of the SPEI-12 maps, computed in August 2022, shown in Fig.1, considering only the negative values and the same color palette of Fig. 4.